C-A/AP/103
July 2003

Beam-optic design considerations for a single-hit microbeam facility for the NASA Space Radiation Laboratory (NSRL) at BNL

P. Thieberger

Collider-Accelerator Department
Brookhaven National Laboratory
Upton, NY 11973

Beam-optic design considerations for a single-hit microbeam facility for the NASA Space Radiation Laboratory (NSRL) at BNL

P. Thieberger

ABSTRACT

The effects of slit scattering in a proposed relativistic heavy ion micro-beam system are investigated through a finite-element beam transport simulation based on TRIM scattering estimates [1), 2)]. In the example used, a long (10 m) distance is chosen between the object jaws and the image to minimize the transmission of scattered ions and the strength of the required quadrupole lenses. A quadrupole triplet configuration is optimized for maximum and equal demagnification in both planes. The impact of beam-energy spread, power supply ripple and lens aperture on the quality of the image are studied for this example, in addition to the multiple scattering effects and their dependence on collimator-jaw surface quality.

A single-hit microbeam facility would be desirable for the NASA Space Radiation Laboratory (NSRL) recently commissioned at Brookhaven National Laboratory (BNL) to investigate the effects of single ion impacts on individual cells or cell-nuclei. As discussed below, the challenges posed by high-rigidity (13 Tm) beams are mitigated by the very low-intensity requirements.

The design goals are:

- One hit per request (one or two per spill).
- Negligible number of multiple hits.
- Few missed requests.
- Beam focused to a $10\mu \times 10\mu$ square or smaller.
- Negligible probability of degraded, fragmented or sputtered ions in the 10μ square.
- Small probability of degraded or fragmented ions on rest of sample.

The main challenges we face are

- Large maximum beam rigidity (13 T m)
- Long stopping ranges in collimator materials for both beam ions and breakup products (in tungsten these ranges are 25.4 mm for 1 GeV/amu Fe and 307 mm for 1 GeV protons)
- Large cross sections for beam scattering and breakup
- Chromatic aberration due to 0.5% momentum sweep during slow extraction

We will show here that most of these problems can be helped very considerably by adopting a beam-optic design with an unusually long object-to-lens distance of the order of 10m, a small lens aperture of the order of 0.5 mm, and taking advantage of the full brightness available from the Booster.

First lets see if such a geometry is realistic in terms of available beam intensity and emittance. Lets assume an object aperture of $(0.1\text{ mm})^2$, a 95% geometric emittance of 5 π mm mrad in each plane [3)] and 10^9 ions per spill. For the x, x' plane, for example, 95% of the beam corresponds to a distribution extending to ± 2.23 σ both in x and x', so $\sigma_x \times \sigma_{x'} = 5/2.23^2$ mm mrad = 1.0 mm mrad. And also $\sigma_y \times \sigma_{y'} = 1.0$ mm mrad. For a 4-dimensional Gaussian distribution, the differential beam intensity can be written as:

$$dI = I_o \ [1/(4\pi^2 \ \sigma_x \ \sigma_{x'} \ \sigma_y \ \sigma_{y'})] \ \exp\{(-1/2)\,[(x/\sigma_x)^2 + (x'/\sigma_{x'})^2 + (y/\sigma_y)^2 + (y'/\sigma_{y'})^2]\} \ dx\, dx'\, dy\, dy'$$

In our example:

$I_o = 10^9$ per spill
$\sigma_x \ \sigma_{x'} = 1.0$ mm mrad
$\sigma_y \ \sigma_{y'} = 1.0$ mm mrad
dx = 0.1 mm
dx' = 0.5 mm/10m= 0.05 mrad
dy = 0.1mm
dy' = 0.5 mm/10m = 0.05 mrad

Therefore in the center of the distribution, i.e. around x = y = 0 and x' = y' = 0 we get:

$$dI = 10^9 \ \times \ 1/(\,39.5 \text{ mm}^2 \text{ mrad}^2) \ \times \ 2.5\times10^{-5} \text{ mm}^2 \text{ mrad}^2 = \ 633 \text{ ions per spill.}$$

This isn't a bad number. If a "beam on-beam off" switch is implemented with an opening and closing time of a microsecond or two, which should be easy, the probability of an ion arriving during a transition is small, and yet one would have an average waiting time of less than 2 ms for a hit after which the switch is immediately closed. On the other hand there is also some room left for even further increase in the aperture-to-lens distance, or a further decrease of the apertures, or beams of lower intensity from the accelerator.

Now that we have seen that the proposed geometry would work, lets analyze the advantages and disadvantages of such an arrangement. The first and most obvious advantage of long systems is that, for a certain required demagnification factor from object-aperture to image, the focal lengths of the lens elements will scale as the overall length, or equivalently the lens strength will scale inversely to that length. This is an important advantage because our maximum beam rigidity of 13 Tm is much higher than for any existing microbeam system, and the design and fabrication of very strong high gradient highly precise microbeam quadrupoles is by no means trivial or cheap.

To obtain a sense of the required lenses, a series of beam optic calculations were performed by implementing simple Excel simulations, first for thin lenses and later for realistic lens elements of finite length. Using Excel's "Solver" it was then easy to find and optimize solutions. For these examples, we tried to use quadrupole singlets that are part of a quadrupole doublet lens we had previously purchased for microbeam work at the Tandem, i.e. for much lower rigidity beams. It turned out that these lenses would indeed be too week for the 13 Tm beams, even for a total object-to-image distance of 10m, but they would work for ~18m. Also, the use of a doublet always results in unequal demagnification factors in both planes. We therefore added a third lens in the simulation, required maximum and equal demagnifications, and allowed the positions of the singlets as well as their strengths to vary, with the constraint of not exceeding the strength of the two existing "Dyer" elements. The result is shown in Figs. 1a and 1b, and the parameters of the lenses are summarized in Tables 1 and 2.

The lines in Figs. 1a and 1b represent paraxial rays, in the x- and y-planes, which start at the center of the object aperture and enter the lens at the radius defined by a 1 mm diameter aperture placed just ahead of the first element. Fig. 1b simply expands the view of the last 1.6 m, and shows the position and length of the singlets as black lines. These positions and lengths (L) are listed in table 1, together with the parameters K1 defining the lens strengths per unit length and the focal lengths f:

$K1=(1/Brho)(dB/dr) \ \{m^{-2}\}$.

f = 1/(K1*L) {m}.

The negative K1 and f values indicate that the element is defocusing in x. A length of 10 cm was chosen for the central element compared to the 6 cm lengths of the other two. This resulted in a slightly smaller K1 value. For equal K1 values, the length of the central lens would have been ~9.3 cm. In any case we see that this central singlet could have a similar design than the other two, only ~50% longer. We see that a demagnification factor of 13.5 is achieved with this arrangement which would result in a beam spot width of 7.4μ for a 0.1mm object aperture. The fact that these lenses are relatively weak could be used to reduce the spot size further by choosing stronger ones.

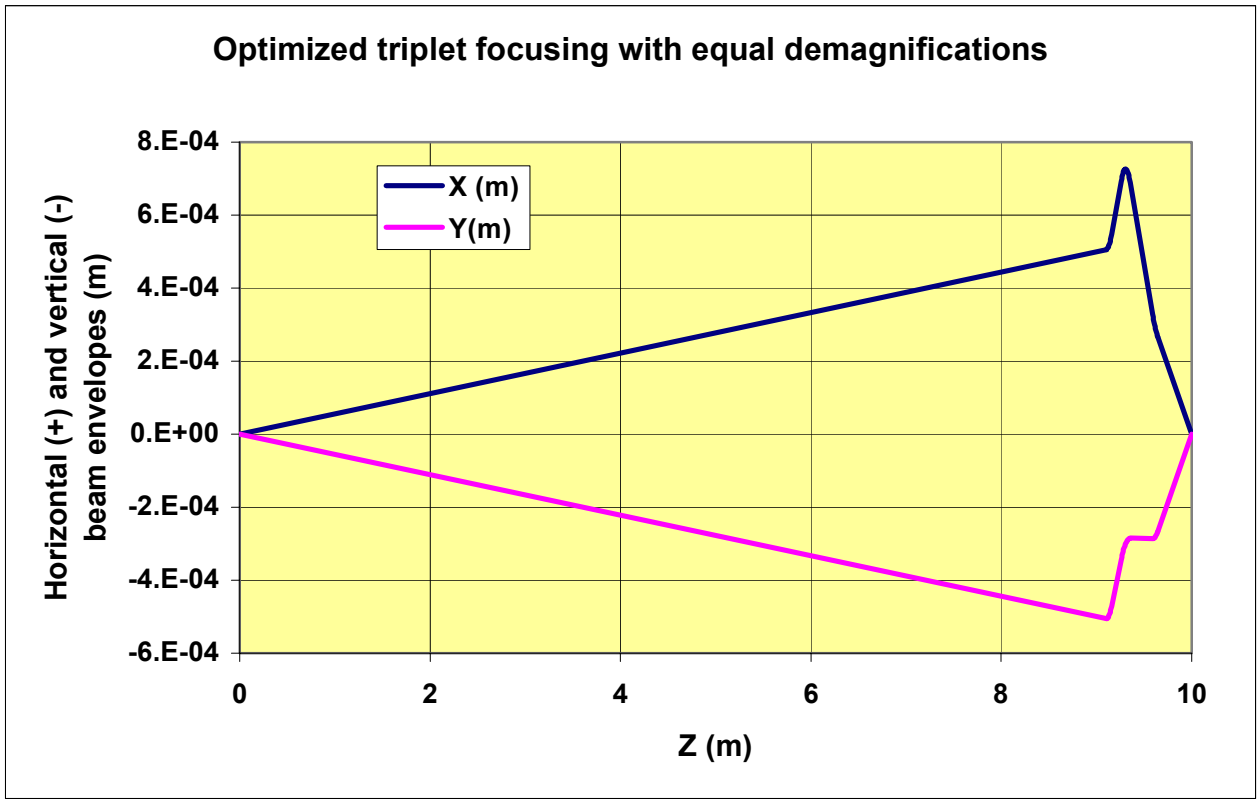

Fig 1a

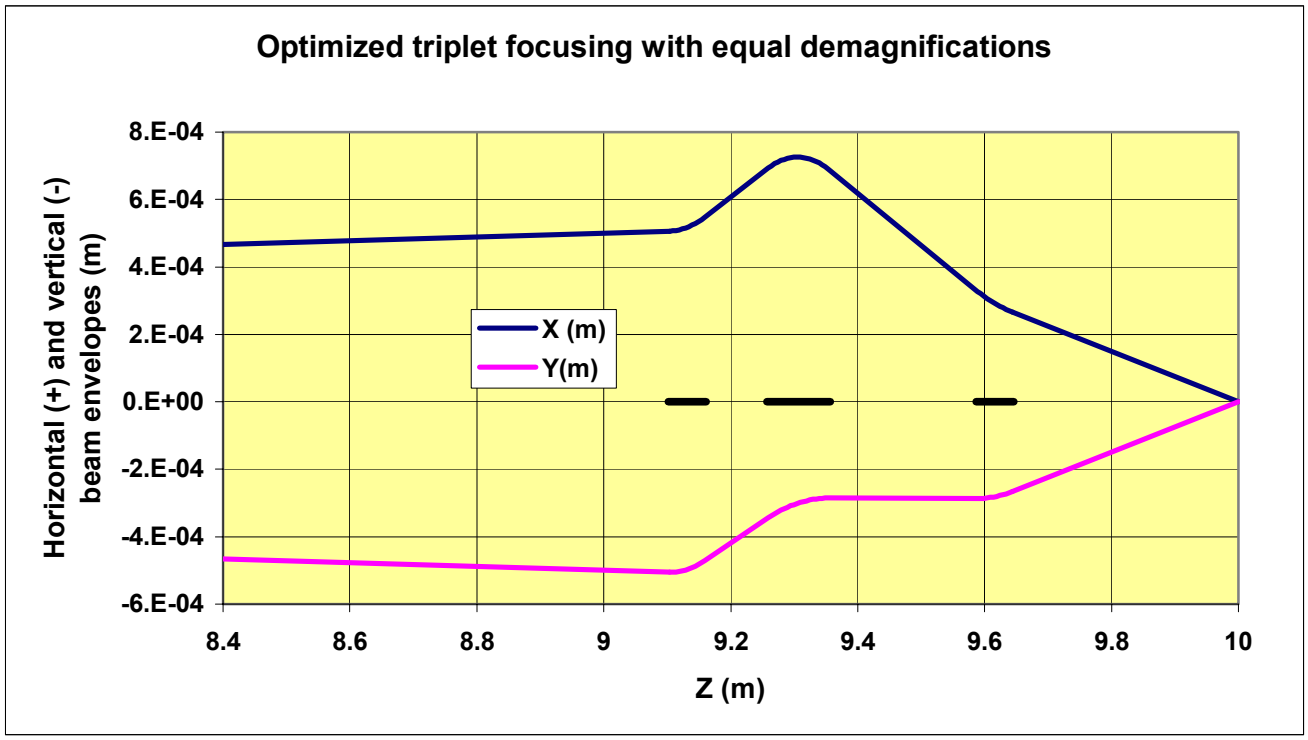

Fig 1b

Table 1 - Lens Parameters

The object aperture is at Z=0 and the image plane at Z=10m

Quadrupole #	K1 (1/m^2)	Focal length (m)	Length (m)	Z start (m)	Z end (m)
1	-45.000	-0.37	0.060	9.1012	9.1612
2	42.093	0.2375	0.100	9.2567	9.3567
3	-45.000	-0.37	0.060	9.5866	9.6466

Table 2 – Image characteristics

	Demagnification factor	Spot size sweep for 1mm lens aperture (μ)	Spot size sweep for 0.5 mm lens aperture (μ)
X	13.45	3.94	1.97
Y	13.45	1.59	0.80

Due to the 0.5% momentum sweep during slow extraction, the focal point will move along the z-axis resulting in a periodic growth and shrinking of the beam spot on a fixed target. That is what is meant by "spot size sweep" in Table 2. This spot size sweep is proportional to the size of the beam in the lens and we assumed that the beam is optimally focused at the center of the momentum sweep. Therefore, in the above example, for a lens aperture of 0.5 mm and neglecting other aberrations, the beam spot will start at $7.4 + 1.97 \approx 9.4$ μ, will then shrink to 7.4 μ in the middle of the sweep and again grow to 9.4 μ . We also see from Table 2 that the maximum of 10μ would be exceeded for a 1 mm lens aperture.

We turn now to the problem of estimating the contamination of the desired beam spot with a continuum of more or less degraded scattered beam particles, beam breakup products and ions sputtered from the collimators. Some detailed simulations are shown later. Here we only discuss the problem qualitatively, and describe measures that will be useful in mitigating these effects, one of which is the adoption of the high beam brightness - small solid angle approach we propose.

As with any collimation problem, "edge scattering" becomes more severe the smaller the aperture simply because the ratio of "edge" to useful aperture increases linearly. While real collimators will probably consist of juxtaposed horizontal and vertical slit systems with adjustable jaws, we can simplify the problem here by just thinking about square or rectangular holes as shown schematically in Fig. 2. While the "edge" is not that well defined for particles that can penetrate deeply into the material, the thickness of the plate will be chosen to be larger tan the range, and therefore trajectories of scattered particles such as #2 and #3 will necessarily be partly in the aperture. Therefore the above argument for the ratio of unperturbed to scattered particles being proportional to the lateral dimension of the hole will roughly hold, even down to very small apertures.

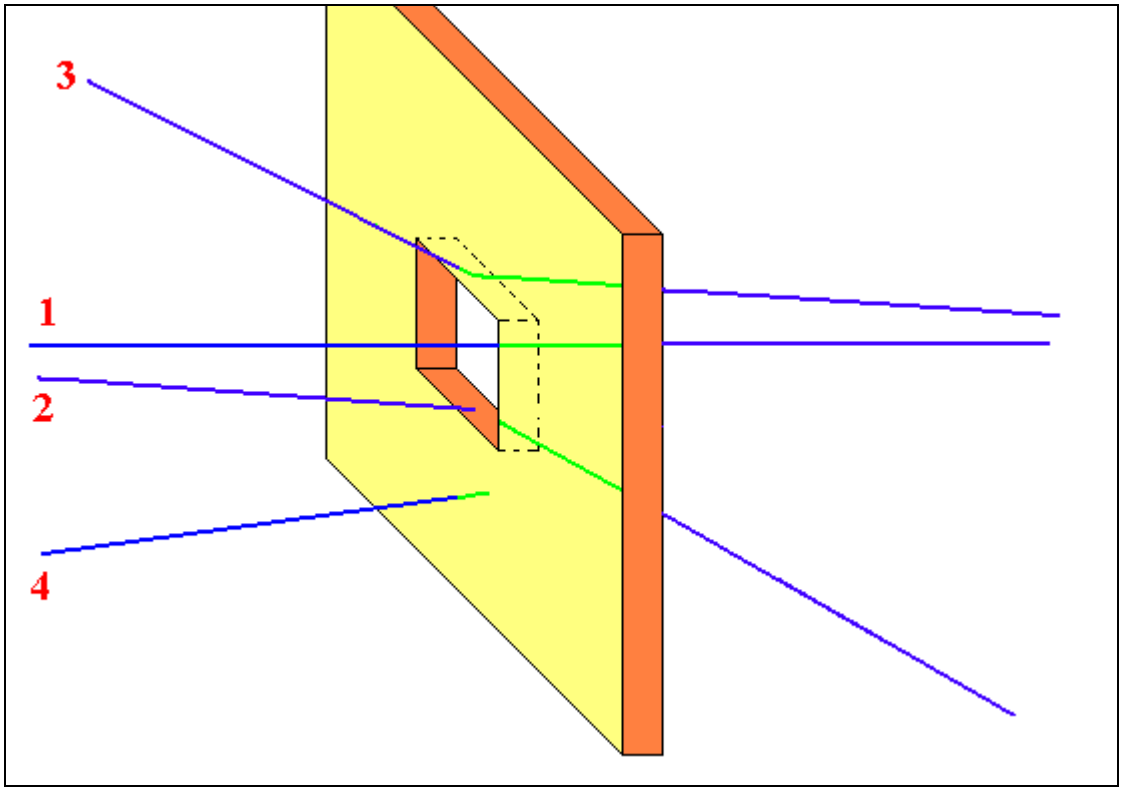

Fig. 2

A large fraction of the background-causing ions will be such as particle #3 in fig. 2 which start out at a steep angle, far outside of the acceptance defined by the object and lens apertures, but which are scattered into this acceptance. Such ions can be largely eliminated by preconditioning the beam before it reaches the object aperture, either by an additional aperture or by appropriate defocusing. These two approaches are schematically illustrated in figs. 3 and 4 respectively.

In the system shown in Fig. 3, the beam transport upstream of the microbeam system is tuned to produce waists in x and in y at the object aperture. A field-limiting aperture placed close to the last focusing element of the conventional beam transport eliminates most of the particles that would impinge on the object aperture at or close to the opening but with angles larger than the acceptance of the micro-lens aperture. Thus a large fraction of the potentially background-generating ions are eliminated. One potential disadvantage of this type of arrangement is that additional longitudinal space is required for a system already envisaged to be fairly long.

An alternative possibility is shown in Fig. 4 were the beam is not focused to a waist at the object aperture. All ions will hit the aperture plate but most of the ones with the wrong angles will hit far from the aperture, i.e. where they have no chance of being scattered into the acceptance. Even though the beam is defocused on the object aperture the acceptance phase-space, indicated by the small square at the origin of the x, x' phase-space diagram, is so small that no intensity penalty is incurred. The areas of the x and y phase space ellipses are the same as when the beam is focused. Therefore the intensity per mm^2 $mrad^2$ at the very center is the same. To what extent such an arrangement may be effective will need to be tested for specific cases by performing detailed ray-trace simulations.

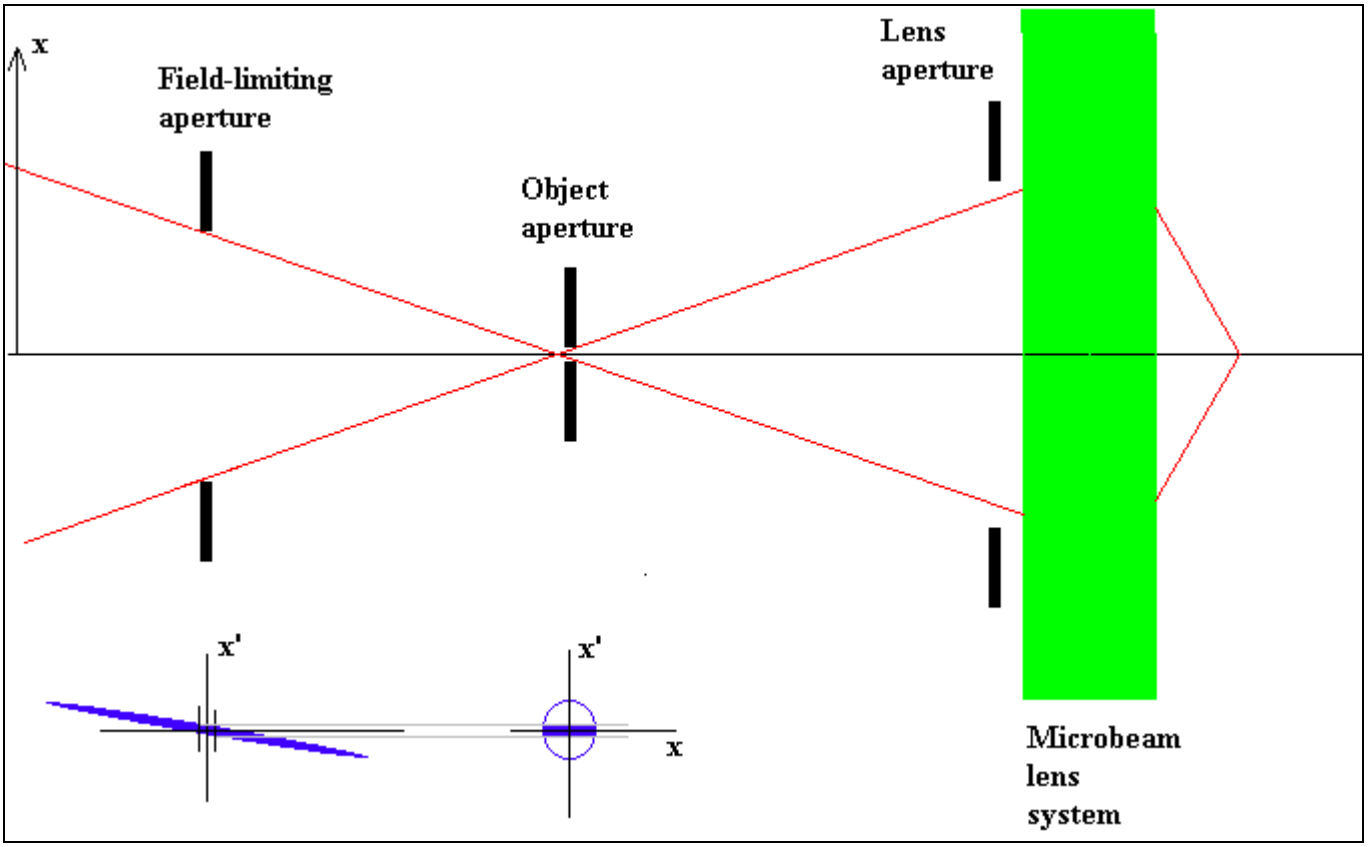

Fig. 3

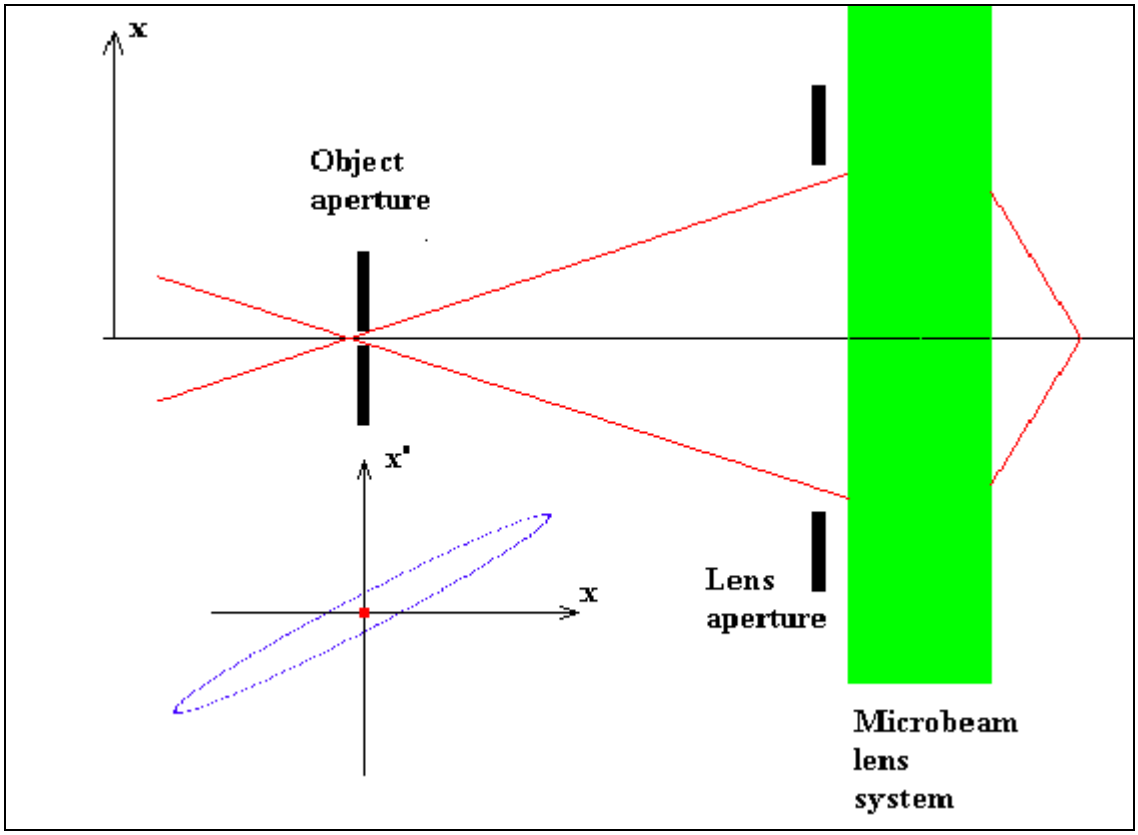

Fig. 4

The entrance angle limiting arrangements described above would be about equally effective for high and for low brightness systems where the low brightness is achieved by purposely increasing the emittance. To see this we assume a constant object aperture width, e.g. 0.1 mm and the same demagnification factor, e.g. 10, in both cases. To maintain the same intensity, for the low brightness case the angular acceptance would need to be larger, but in the same measure as the emittance. Therefore the above considerations apply equally for both types of systems. The number of scattered particles produced in the object aperture can be very considerably reduced in both cases, and the resulting ratio of scattered ions to useful beam is about the same.

Only small fractions of these scattered particles will make it through the lens aperture, but these fractions are now very different for the high brightness and low brightness cases. The angular distribution of the scattered ions and fragments is much wider than the angular distribution of the primary beam, and nearly the same for both situations. Therefore the number of transmitted scattered particles and fragments will be roughly proportional to the angular acceptance while the number of primary ions transmitted is the same. We therefore see that, for a constant beam-on-target intensity, the ratio of useful-to-background particles scales roughly as the brightness of the beam.

Fig 5 illustrates schematically the fact that the ratio of non-scattered to scattered particles accepted through the lens aperture roughly scales as the square of the length of the system.

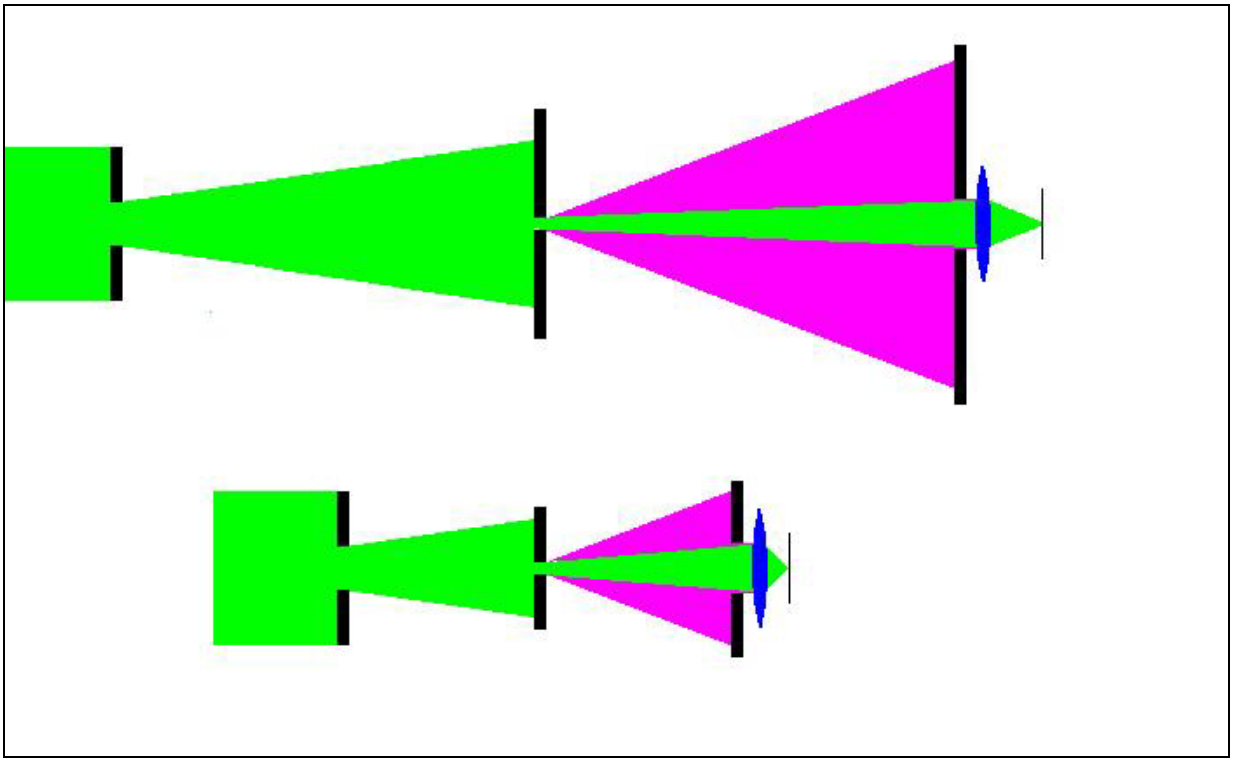

Fig 5 Schematic comparison of two systems differing only by a factor of 2 in length.

The measures proposed above will reduce the background by orders of magnitude, but to know whether this reduction will be sufficient will require detailed simulations and experiments. If more cleanup is needed, the proposed geometry lends itself to a further possible remedy, namely the introduction of a magnetic dipole deflector immediately following the object aperture taking advantage of the generally lower rigidity of the contaminants. Such a dipole may need to be extremely stable, to an extent that may make it difficult to implement

The proposed geometry, with the long object-to-lens distance, the small lens aperture and the field-limiting aperture also makes the beam on off switching easy. A small and fast magnetic or electrostatic deflector located just before or after the object slits will suffice.

To implement such a long, high brightness, microbeam system, in addition to counting with the required space, one also needs a conventional beam line from the accelerator which is sufficiently stable, free of thick absorbers and well instrumented to transport and preserve the high brightness beam. Also a long relatively vibration-free table will be required to mount the apertures and lenses. This can probably be accomplished by using a large I-beam, such as used in the construction industry, appropriately decoupled from the floor.

In conclusion, the available brightness of the slow-extracted Booster beam is a valuable commodity which, if preserved, would be very helpful in specifying lenses of adequate quality and strength at a reasonable cost, in producing beams relatively free of contamination and in easily implementing fast switching, all required for almost instantaneous and clean delivery on-demand of single ions on a 10μ or smaller beam spot.

Results from first TRIM-based simulations

A simple specialized ray-trace program (MicroTracer) was written to simulate systems such as the one shown in fig. 3. Only multiple scattering in the object aperture jaws has been implemented so far. Also, the TRIM [1), 2)] results used may need to be revised once a new version of TRIM becomes available[4)] which will more accurately calculate the stopping of relativistic ions [5)].

The simple aperture in fig.3 was replaced by a set of horizontal jaws followed by vertical jaws as shown in fig. 6

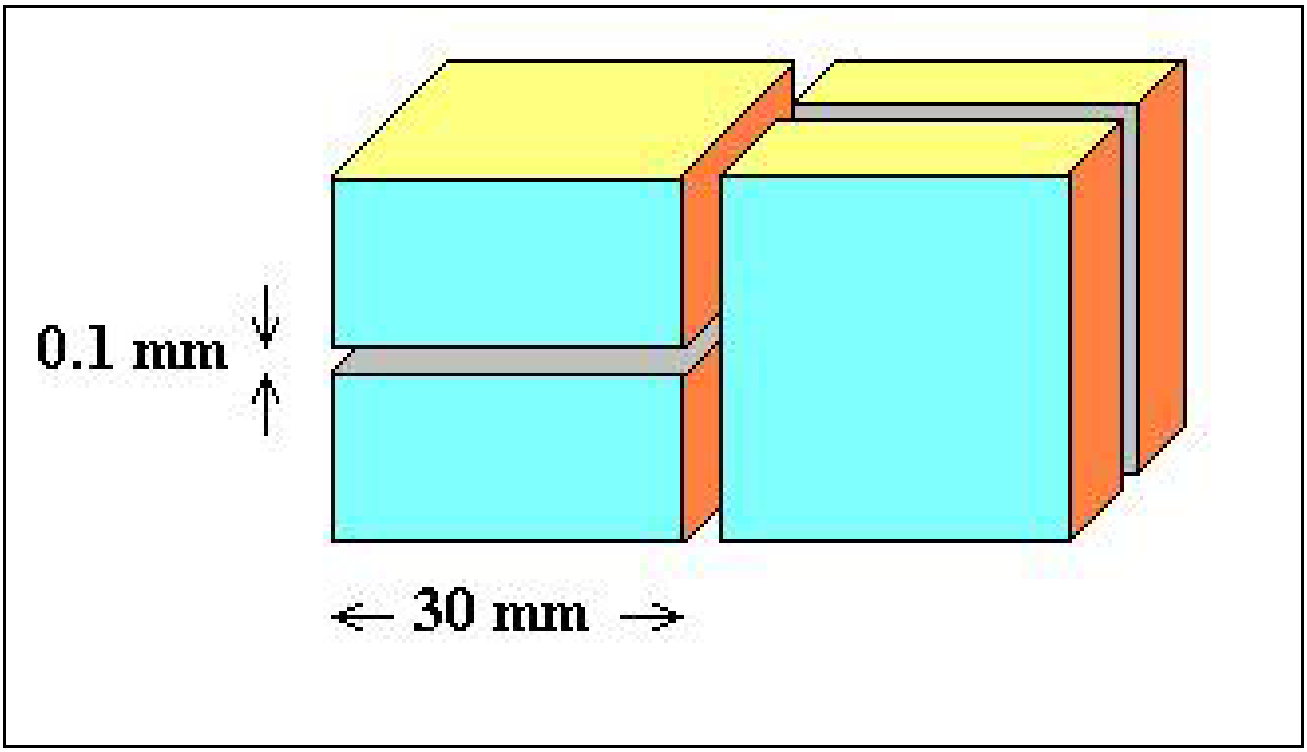

Fig. 6 Schematic of the tungsten jaws used for defining the object aperture.

The material used for the calculations is tungsten, and the length of 30 mm was chosen to be slightly larger than the 26 mm range of 1 GeV/amu iron in tungsten. For the calculations, each set of jaws was divided into 300 vertical slices, each 100 microns thick. A particle traversing one of these slices looses energy and is displaced from its original trajectory by lateral offsets and by angular increments. All these quantities are statistically distributed as simulated by TRIM. Table 3 is an example of the TRIM output for the first ten 1 GeV/amu iron ions emerging form a 0.1 mm thick tungsten absorber.

Using TRIM repeatedly as a subroutine in our ray trace program would be difficult and very time consuming. The alternative we used is to pre-calculate 2000 iron ion traversals through 100 micron-thick tungsten for 55 energies ranging from 2 to 56 GeV. Our calculation then uses these traversals in sequence, picking the tabulated energy closest to the actual entrance energy at each slice. The energy of the ion is then decremented by the tabulated amount and the lateral positions and angles are likewise changed before the trajectory through the next slice is computed. MicroTracer of course keeps track of where there is material and where there is vacuum and acts accordingly.

Table 3

TRIM output for ten 1 GeV/amu iron ions transmitted through 0.1 mm tungsten.

```
================  TRANSMIT.txt : File of Transmitted Ions  =================
=  This file tabulates the kinetics of ions or atoms leaving the target.     =
=  Column #1: S= Sputtered Atom, B= Backscattered Ion, T= Transmitted Ion.   =
=  Col.#2: Ion Number, Col.#3: Z of atom leaving, Col.#4: Atom energy (eV).  =
=  Col.#5-7: Last location:  X= Depth into target, Y,Z= Transverse axes.     =
=  Col.#8-10: Cosines of final trajectory.  NOTE: Use hotkey  C  for details.=
= *** This data file is in the same format as TRIM.DAT (see manual for uses).=
========== TRIM Calc.= Fe(56 GeV) ==> 0.1 mm Tungsten(  100 um) =============

 Ion  Atom   Energy       Depth       Lateral-Position        Atom Direction
 Numb Numb    (eV)         X(A)        Y(A)       Z(A)     Cos(X)     Cos(Y)    Cos(Z)

T  1  26 .5584989E+11  1000002E+00  .1996E+03  .3180E+03  .9999990  .0006832  .0012010
T  2  26 .5584736E+11  1000000E+00  .2054E+03 -.2270E+03  .9999999  .0005063  .0000705
T  3  26 .5583167E+11  1000001E+00  .1784E+03  .2621E+02  .9999998  .0004824 -.0002649
T  4  26 .5584518E+11  1000001E+00  .1069E+03  .2315E+03  .9999997 -.0002548  .0007454
T  5  26 .5584069E+11  1000001E+00  .6575E+02  .2281E+03  .9999999 -.0000196  .0004427
T  6  26 .5584388E+11  1000002E+00 -.2258E+03  .3651E+03  .9999997 -.0005116  .0005320
T  7  26 .5583595E+11  1000002E+00 -.1894E+03  .7673E+02  .9999999 -.0002491 -.0000397
T  8  26 .5584476E+11  1000002E+00 -.4234E+03  .2913E+01  .9999999  .0000303 -.0002728
T  9  26 .5584219E+11  1000000E+00  .2868E+03  .1990E+03  .9999997  .0004559  .0005843
T 10  26 .5584895E+11  1000002E+00  .4178E+03 -.1055E+03  .9999997  .0007256 -.0001822
```

One further refinement was introduced, to simulate the roughness of the jaw surfaces, which is expected to have a significant impact on scattering, especially for the very shallow impact angles characteristic of the present geometry. Each slice was modeled as ending in a triangular ridge such as shown in fig. 7

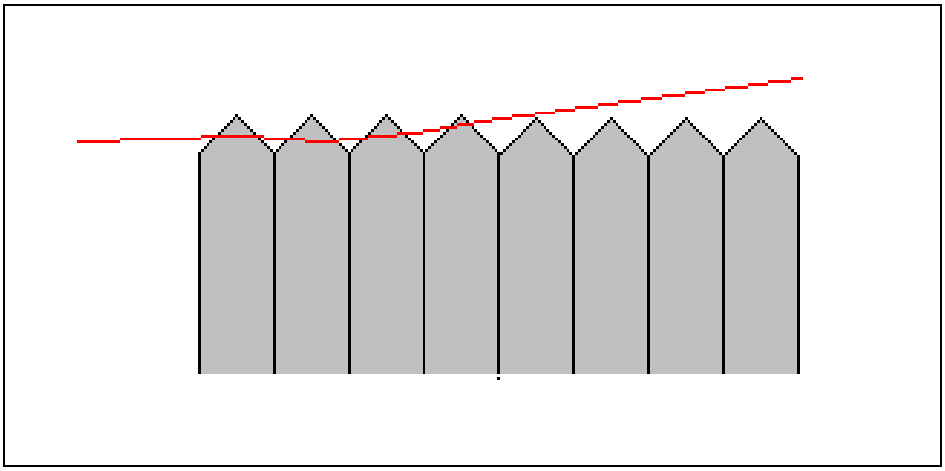

Fig. 7 Schematic of a grazing impact of an ion on the face of one of the collimator jaws. Surface irregularities are simulated by the "picket-fence" cross-section. The figure is not to scale. While the slice thickness used was 100 microns, the maximum peak-to-valley irregularities modeled were 5 microns typical of a normal, well machined but not polished surface.

The height of the "teeth" is an input to the program and can be chosen to be zero to simulate a perfectly smooth surface. When an ion traverses one of these surface teeth, the program reduces the energy loss obtained from the TRIM table in proportion to the ratio of distance traversed in the material to the total width of a slice. The displacement and angle increments are scaled with the square rooth of that ratio.

Before running the program to evaluate the effects of scattering, it was necessary to first test the ray-trace algorithm to verify that it reproduces the beam-optic results obtained previously as shown in tables 1 and 2 and in fig. 1. It was also necessary to establish which ions hitting the collimator jaws have a chance to get through, so as to avoid wasting computer time on a large number of ions that have a negligible chance of emerging. Figures 8 through 16 show the results of these tests, as well as other studies to determine the impacts of defocusing, momentum spread and power supply ripple.

Figs 8a and 8b show the result of transporting 20,000 ions from random locations within the 1 × 1 mm square field aperture to random locations within the 100 × 100 micron square object aperture and then through the lens system defined above to an image plane located exactly at 10 m. We can see that the image seems to be somewhat out of focus.

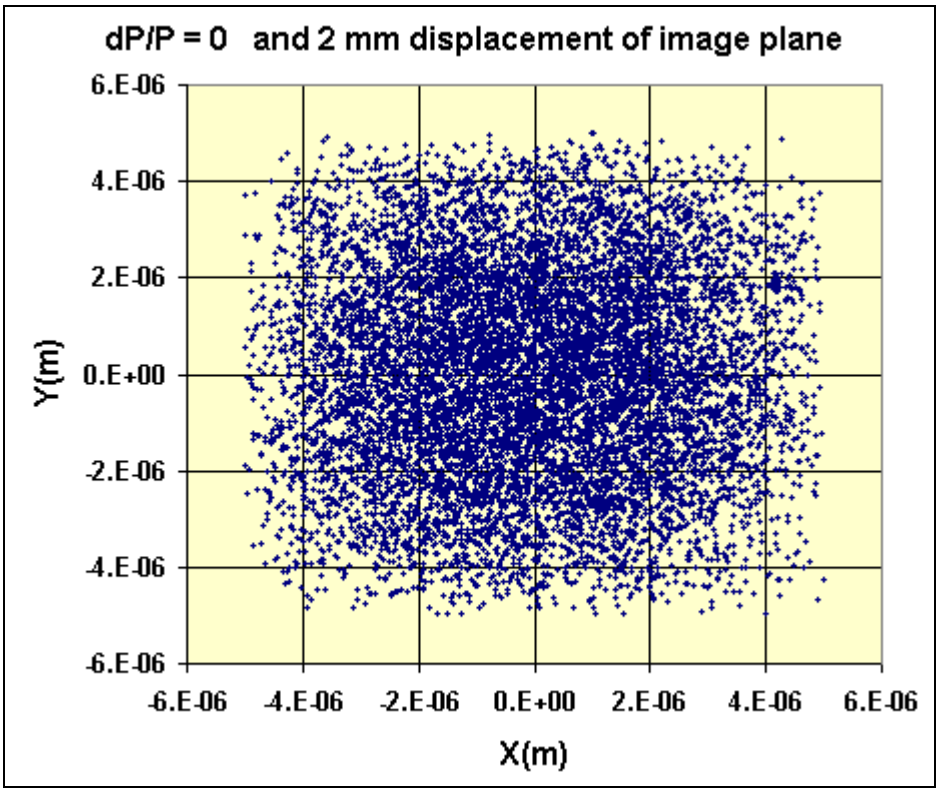

Fig. 8a 20,000 1 GeV/amu iron ions focused onto the image plane located at 10.000 m

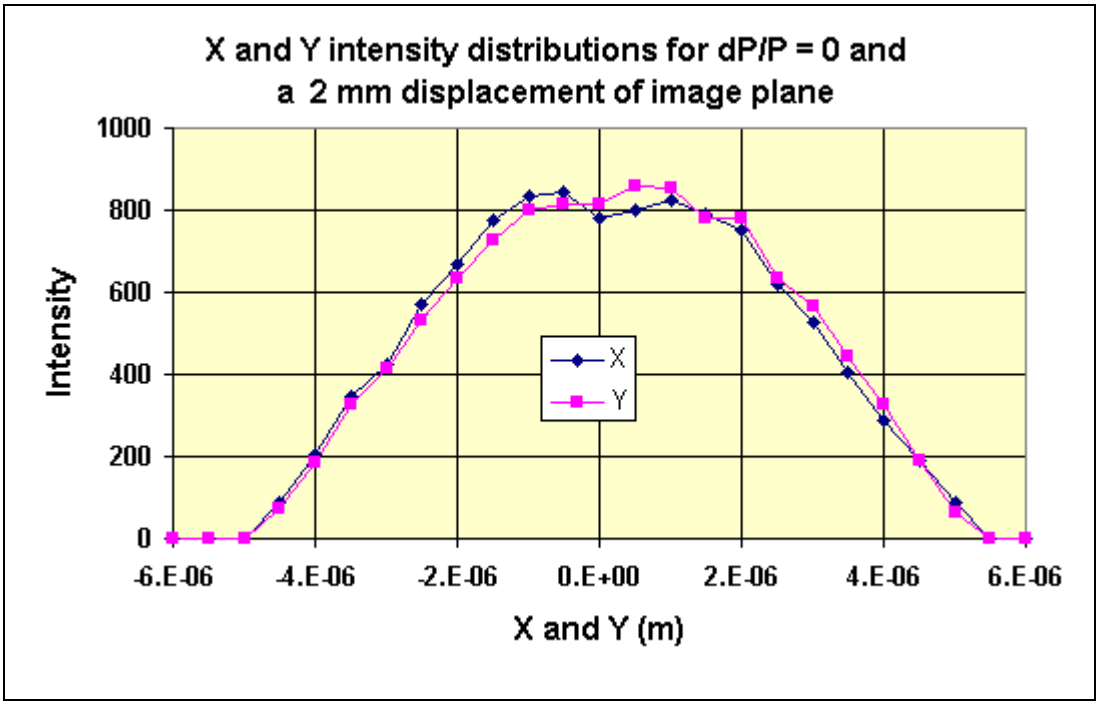

Fig. 8b X and Y projections of the 20,000, 1 GeV/amu iron ions, focused onto the image plane located at 10.000 m

By trial and error it was determined that a much better focus is obtained at 10.002 m, as shown in figs. 9a and 9b. While not identical to the 10 m focal plane predicted by the beam-optic program this location is close enough. We also see from Fig. 9b that the full width of the image is about 7 μ ,which for the object aperture of 100 μ , corresponds to a demagnification factor of 14.3, close but slightly better than the factor 13.45 predicted in Table 2 using the beam-optic program.

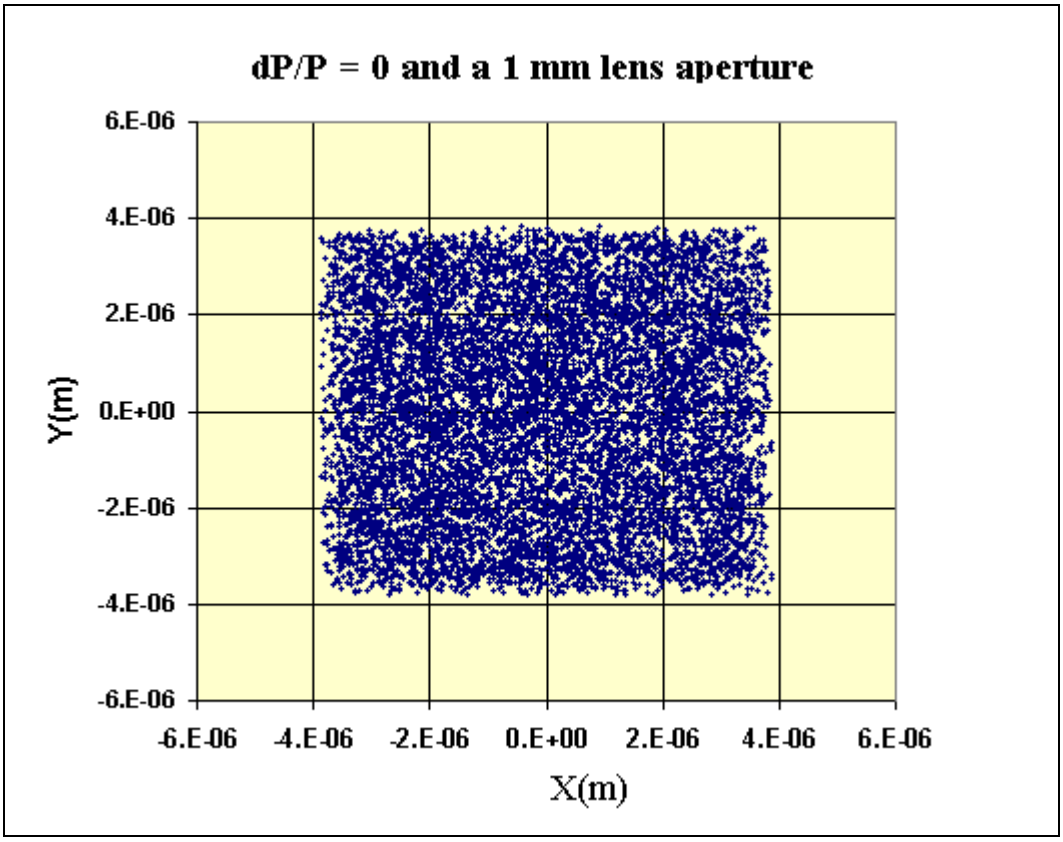

Fig. 9a 20,000 1 GeV/amu iron ions focused onto the image plane located at 10.002 m

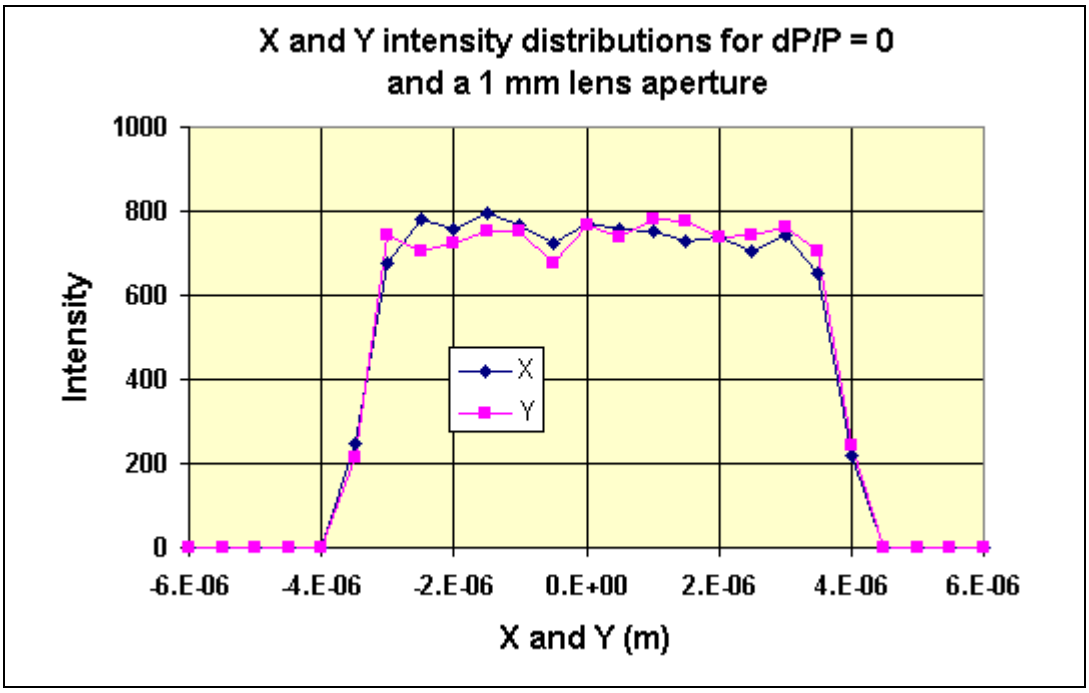

Fig. 9b X and Y projections of the 20,000, 1 GeV/amu iron ions, focused onto the image plane located at 10.002 m

Another feature of the program, not mentioned so far, is that a momentum fluctuation can be specified to investigate the effects of the momentum sweep during slow extraction from the Booster. Figure 9 shows what happens to the beam profiles shown in fig. 9b when there is a 0.5% momentum sweep.

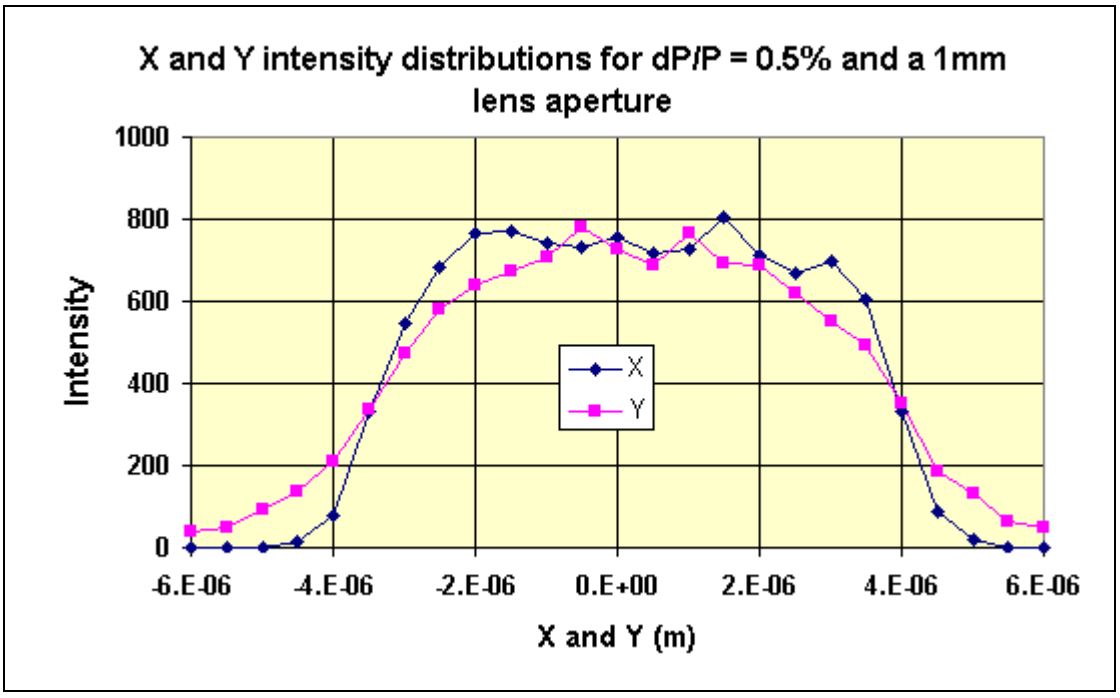

Fig, 10 The defocusing effect of a 0.5% momentum sweep with a 1 mm lens aperture. Compare these profiles with the ones shown in fig. 9b.

This effect is proportional to the lens aperture and can therefore be reduced. Fig. 11 shows the result of reducing the lens aperture to 0.5 mm

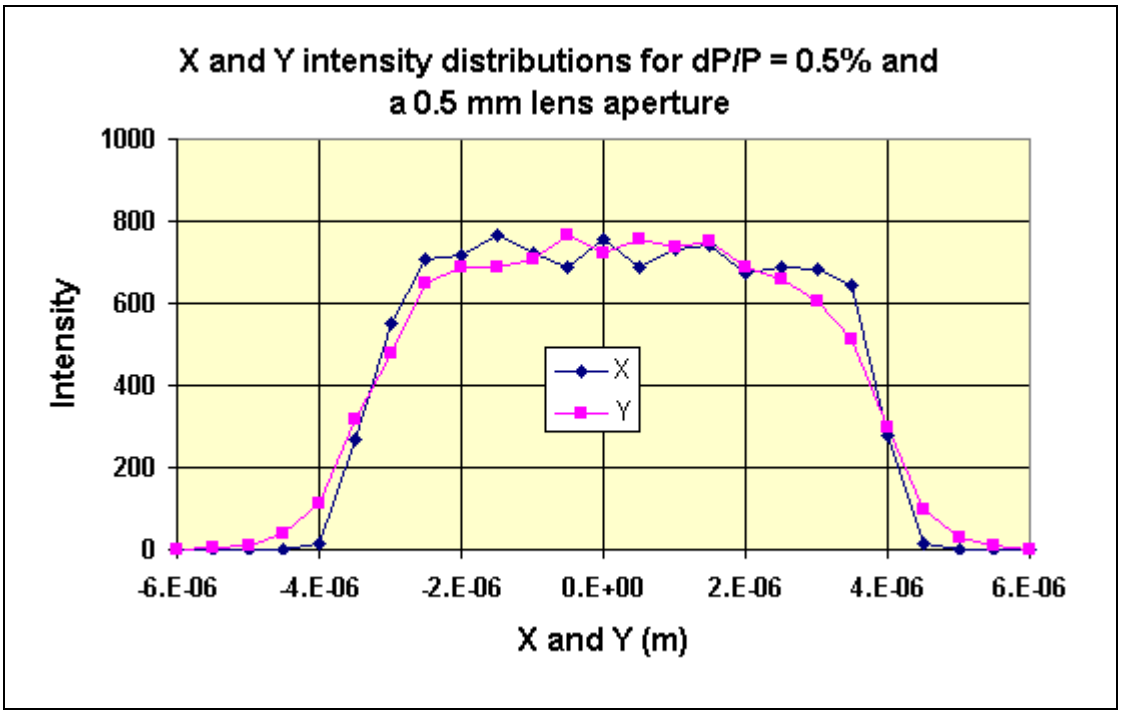

Fig. 11 The defocusing effect of a 0.5% momentum sweep with a 0.5 mm lens aperture. Compare with fig. 10.

The effects observed here are in good agreement with the values of the "spot size sweeps" calculated in Table 2, but the roles of X and Y seem to have been interchanged. This will be investigated further.

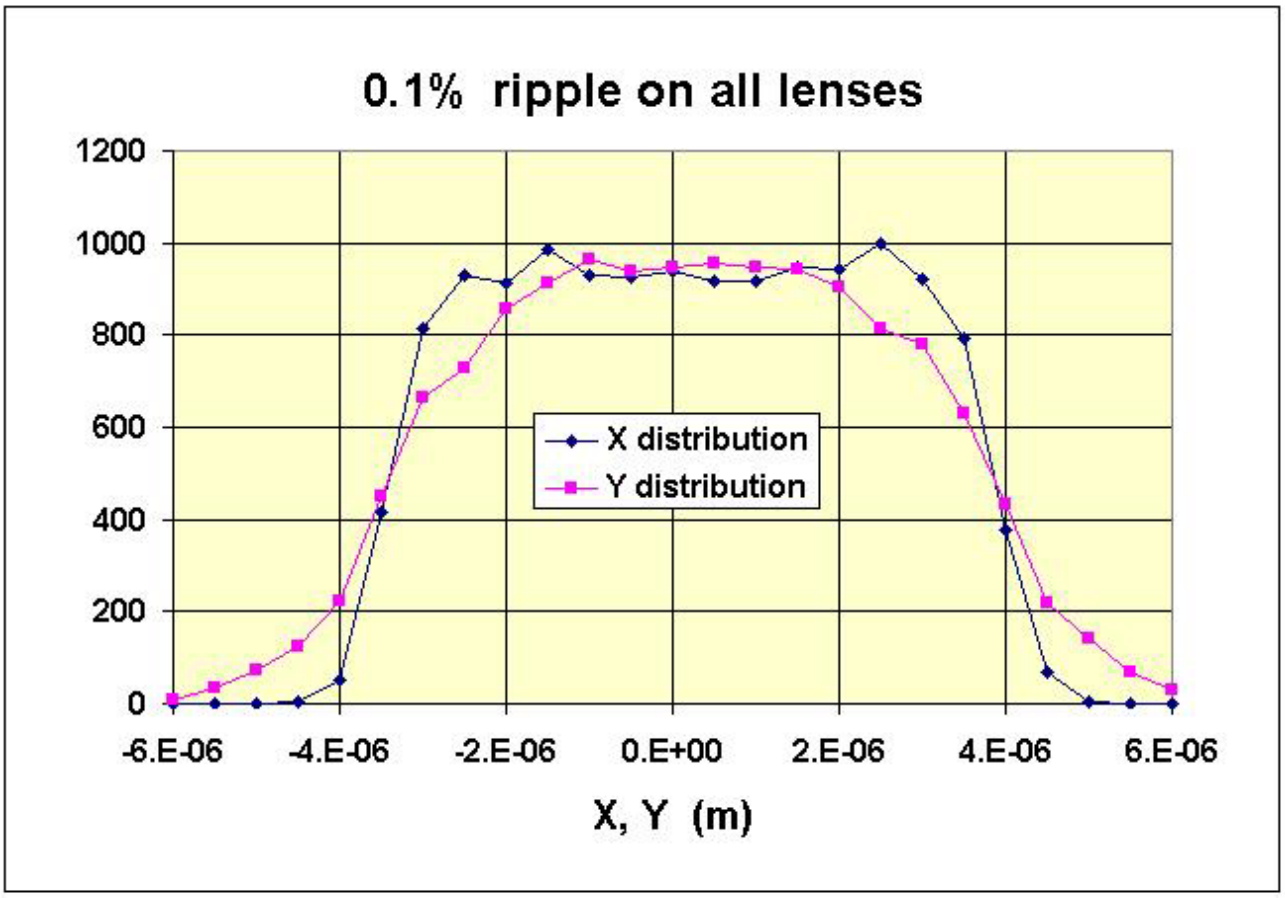

Fig 12 . Calculated Effect of power supply ripple on the quality of the beam spot. This simulation was performed with a 1 mm lens aperture and dP/P = 0. Compare with fig. 9b .

Figure 12 shows an estimate of the effect of 0.1% peak-to peak ripple on all the quadrupole supplies. In the model, the noise phases in the individual supplies are uncorrelated. In reality, 60 Hz ripple will of course be correlated and the final result may be slightly worse or slightly better, depending on phases. However the difference will be small because the main effect comes from the central lens. It will be easy to effectively eliminate this effect with adequately stable supplies (e.g. $dV/V = 10^{-4}$).

MicroTracer normally discards most of the detailed information for each trajectory before calculating the next one, recording only the coordinates of the end point and the energy of the ion before entering the last surface. A special run was performed to see what happens when particles are scattered in the jaws of the object aperture. To that end, ions were aimed from the center of the field aperture to a point of coordinates Z= -3 cm , X = 0, Y = 55 microns. This point is at the entrance surface of the upper horizontal jaw at a Y-coordinate corresponding to the valleys of the corrugated surface as shown in fig. 13a

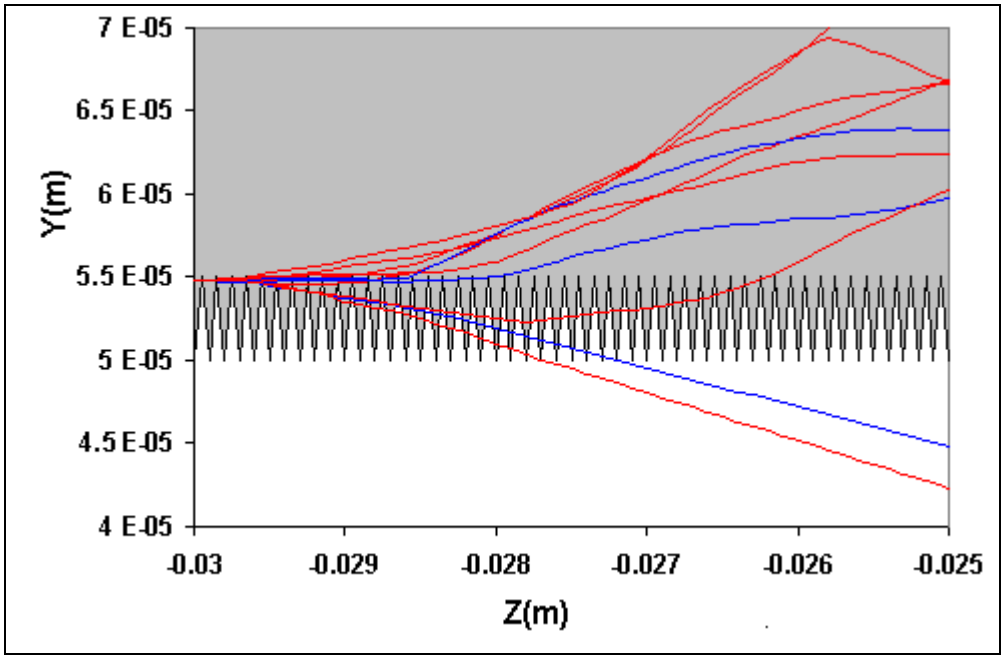

Fig 13a Y projection of the first 5 mm of ten trajectories discussed in the text.

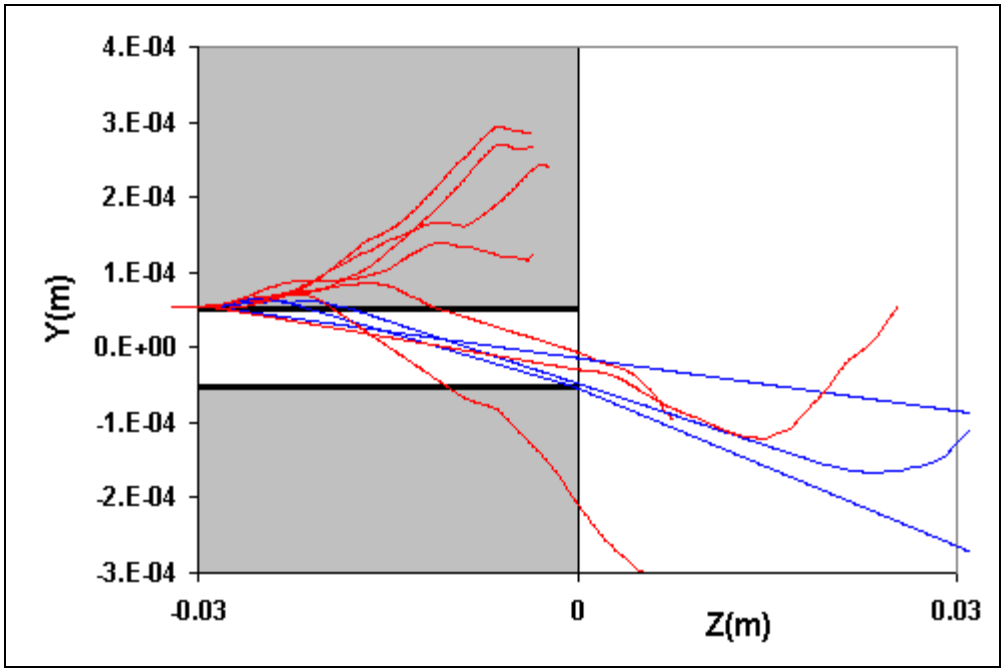

Fig. 13b Y-projection of ten trajectories through the object jaw system.

In fig, 13a we see the first 5 mm of the trajectory's Y-projection and fig. 13b shows the full length of both the horizontal and the vertical jaws. There are ten trajectories plotted. The seven that stop in one of the jaws are traced in red and the three that escape in blue. Figs. 14a and 14b show the corresponding X-projections.

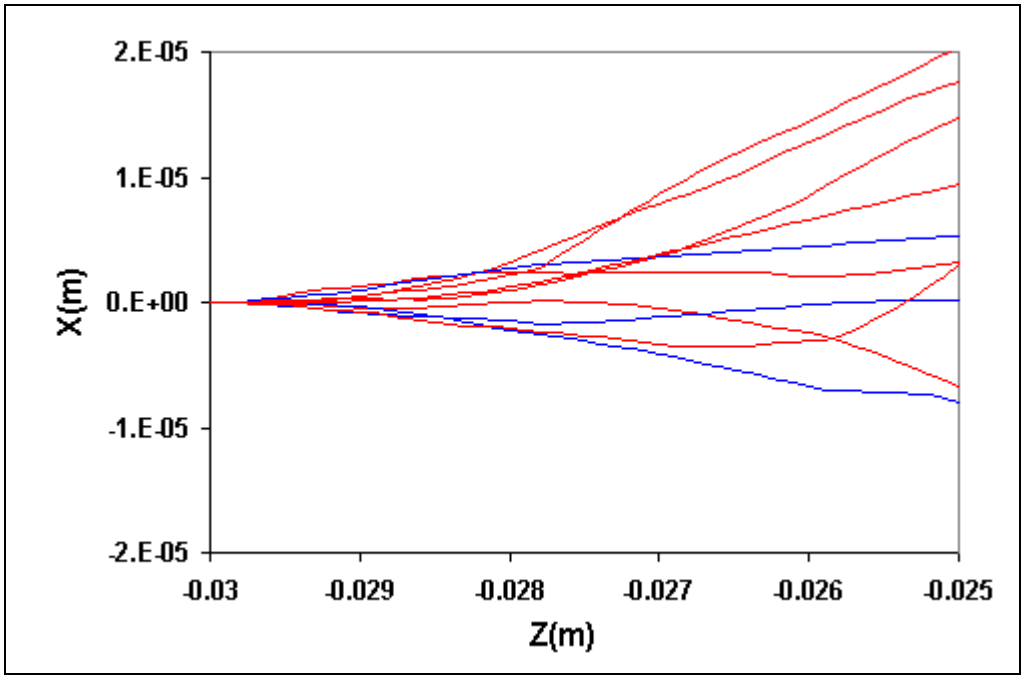

Fig. 14a X-projection of the first 5 mm of ten trajectories discussed in the text.

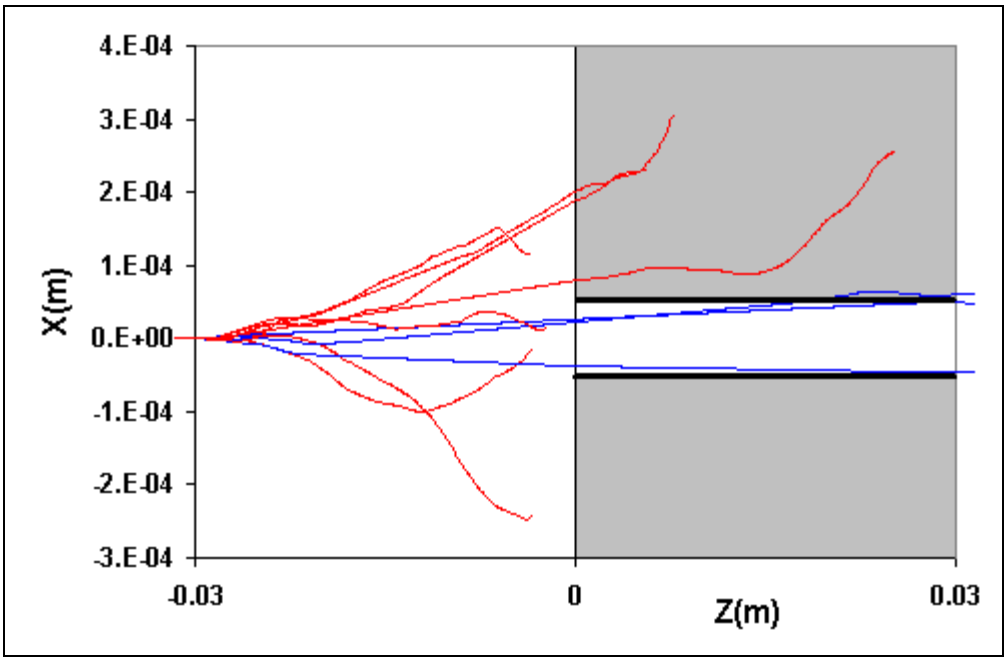

Fig. 14b X-projection of ten trajectories through the object jaw system.

It is worth noting how grossly distorted the scales are used in all the preceding figures depicting the object collimator jaws. A more accurate representation of the small aspect ratio of one of these pairs of jaws is shown in fig.15.

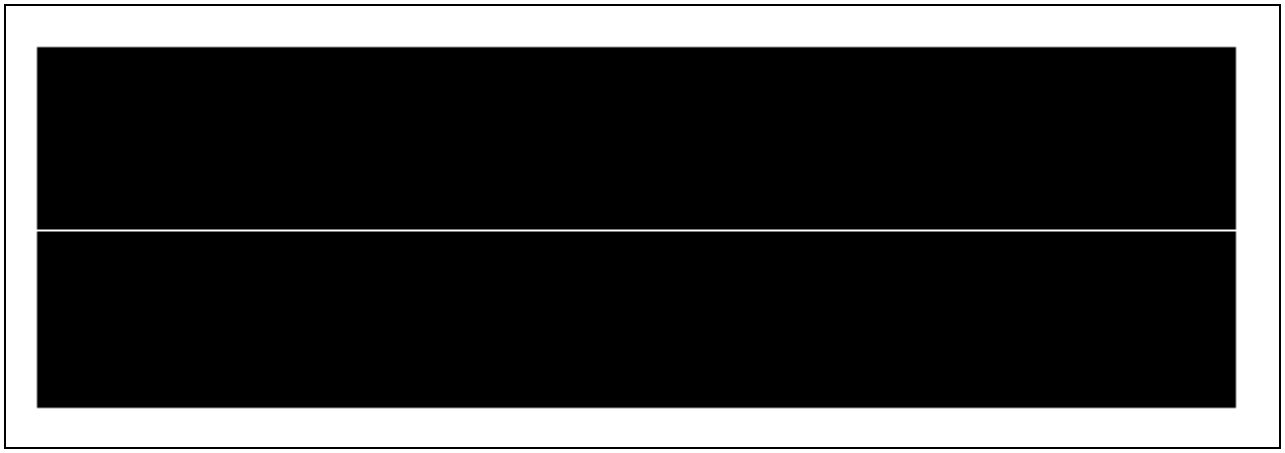

Fig. 15 Realistic representation of the aspect ratio of one of the object gaps.

To avoid wasting time on trajectories that will almost certainly terminate inside the jaws, the next step was to determine the size of the area surrounding the object aperture for which arriving ions will have a significant probability of traversing both sets of jaws. For that purpose an option was included in the program whereby ions originating from random points within the field aperture are aimed exclusively at a thin square "ring" of a specified size surrounding the object aperture defined by the jaws. Obviously aiming at areas inside the object aperture will result in 100% probability for each particle to reach the image plane. But for areas outside the object aperture some ions will end up on the lens aperture and others will stop in one of the sets of jaws, while fewer and fewer ions will make it to the image plane as one moves further away from the center. The results of a series of such calculations are shown in Fig.16.

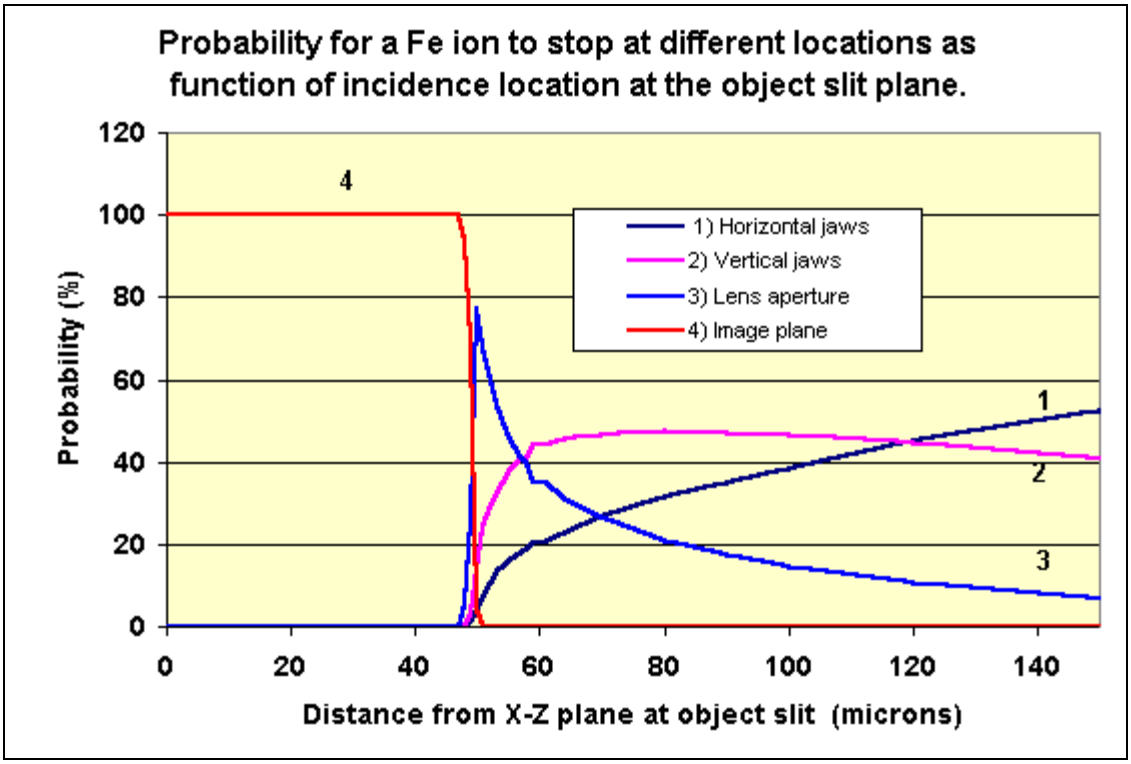

Fig. 16

We see that, if we were only concerned with ions that reach the image plane, it would be sufficient to restrict the calculation to an area only a few microns wider than the object aperture. But to gain a better understanding of the effects of scattering we want to also record impacts on the lens aperture. Therefore the

impact area on the object aperture was chosen to be a 0. 5 × 0.5 mm^2 square centered on the beam axis, which, according to the results of fig. 16 (curve #3), will include almost all the scattered ions that emerge from the object jaws.

Tables 1 and 4 list the parameters used for these calculations. The image plane location is the one listed in table 4 because of the better focus (see figs, 8 and 9). To keep the situation as simple as possible for the scattering analysis, dP/P = 0 was assumed.

Table 4

	Z (m)	Width and height (μ)
Field aperture	-9.0	1,000 × 1,000
Horizontal object jaws	-0.03 to 0	100
Vertical object jaws	0 to 0.03	100
Lens aperture	9.0	1,200 × 1,200
Image plane	10.02	
Impact area on object		500 × 500
DP/P = 0		

Figs. 17a to 17e show the results for jaws with 5μ peak-to-valley surfaces and figs 18a to 18e show the corresponding results for perfectly smooth jaw surfaces. In both cases 200,000, 56 GeV iron ions were launched from random points within the 1 × 1 mm^2 field aperture and aimed at random points within the 0.5 × 0.5 mm^2 object impact area defined above.

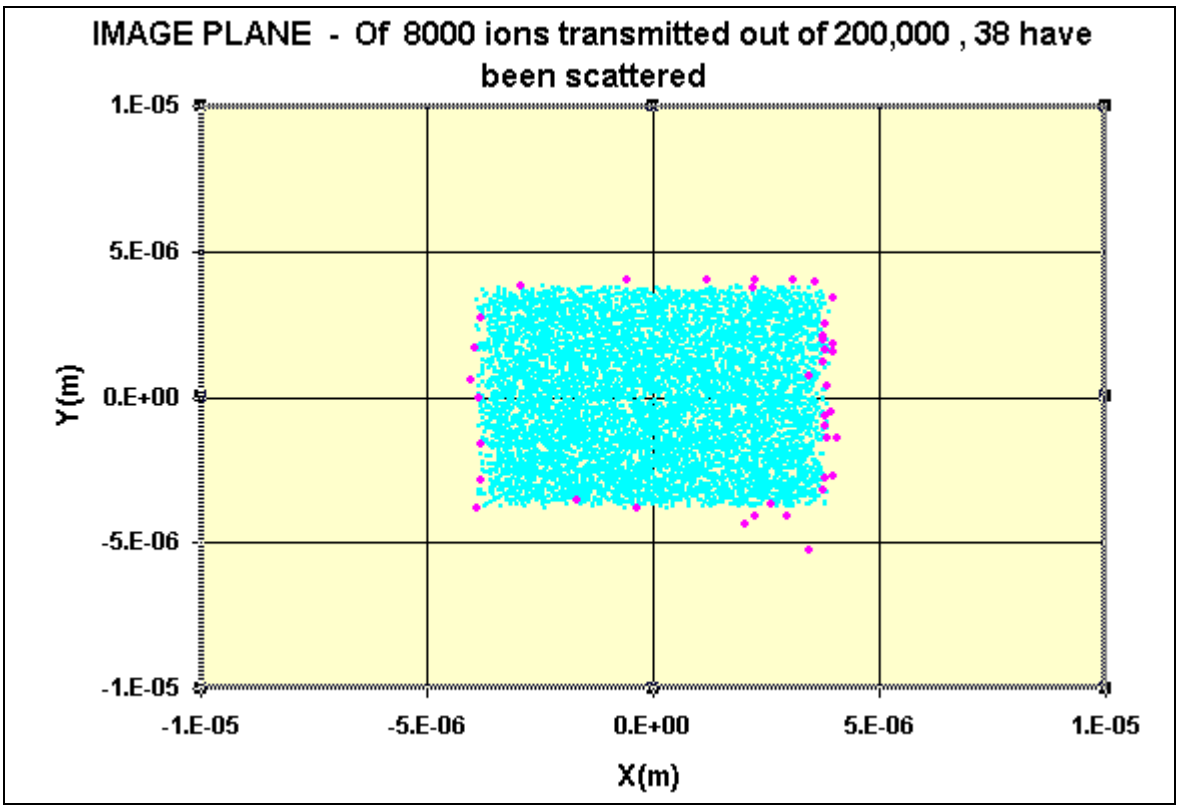

Fig. 17a The ions scattered from object jaw surfaces with 5μ peak-to-valley undulations are shown as larger, purple dots. The energy-loss of these scattered ions ranges from 30 KeV to 25 MeV.

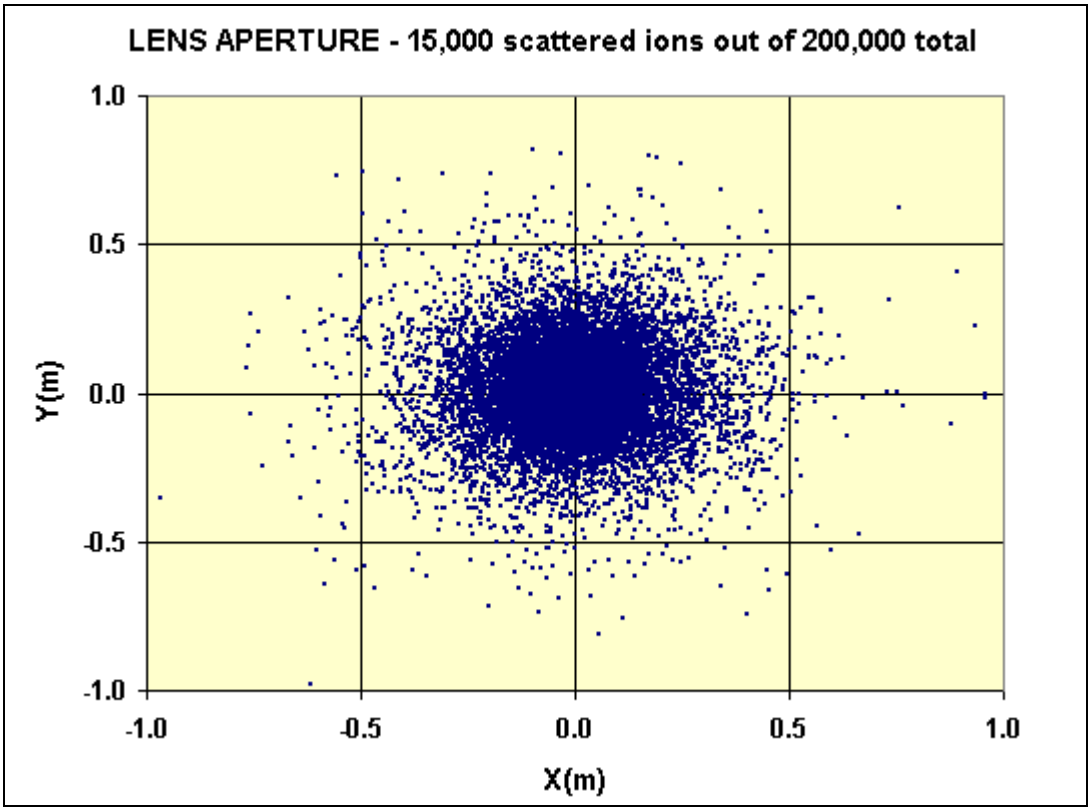

Fig. 17 b Distribution of the ~15,000 scattered ions stopped by the lens aperture for the case in which object jaws with 5μ peak-to-valley surfaces were simulated

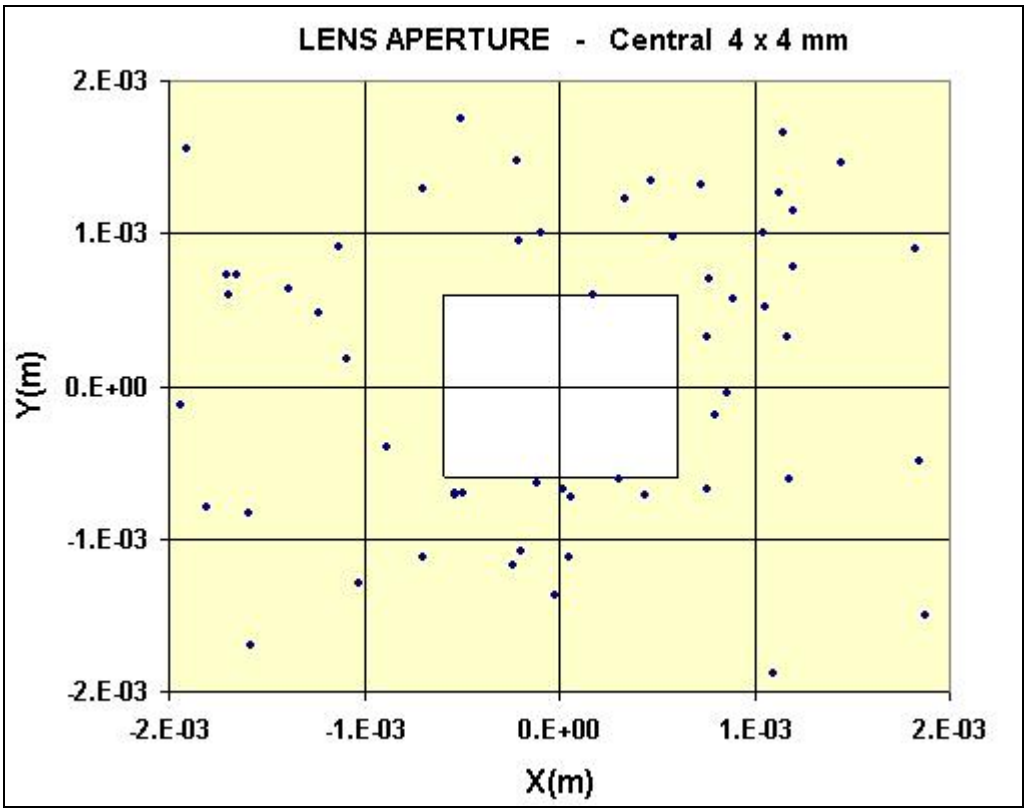

Fig.. 17c The central 4×4 mm^2 of the distribution shown in fig. 17b. The 0.6×0.6 mm2 lens aperture is indicated by the square at the center.

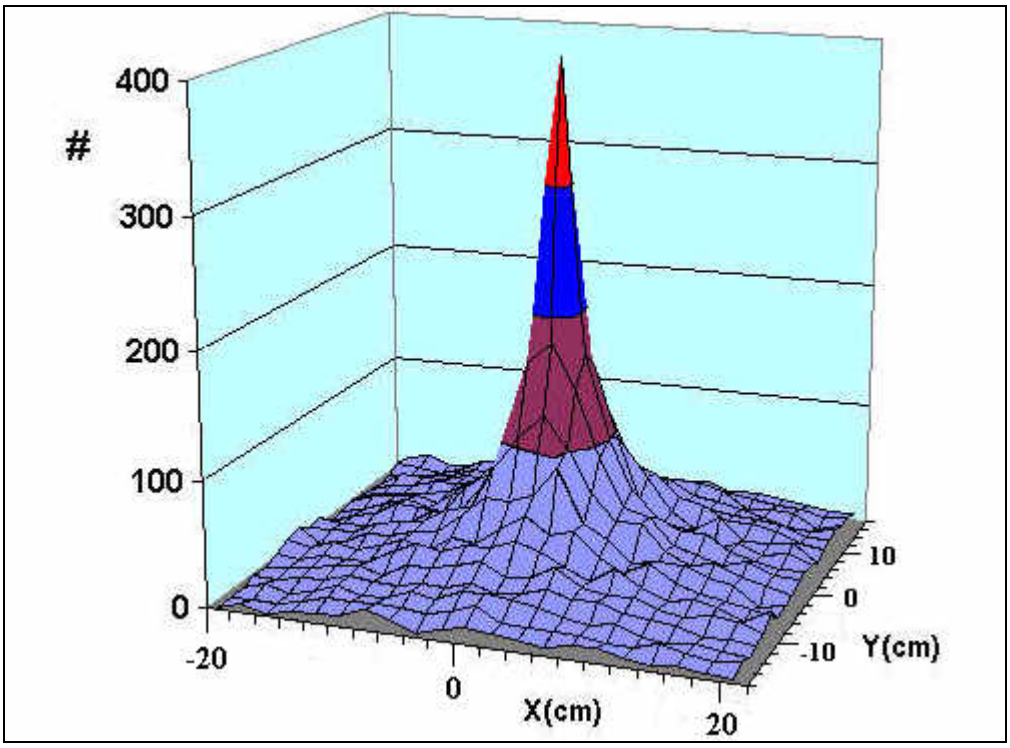

Fig. 17d 3-D view of the distribution of scattered ions stopped by the lens aperture for the case in which object jaws with 5μ peak-to-valley surfaces were simulated.

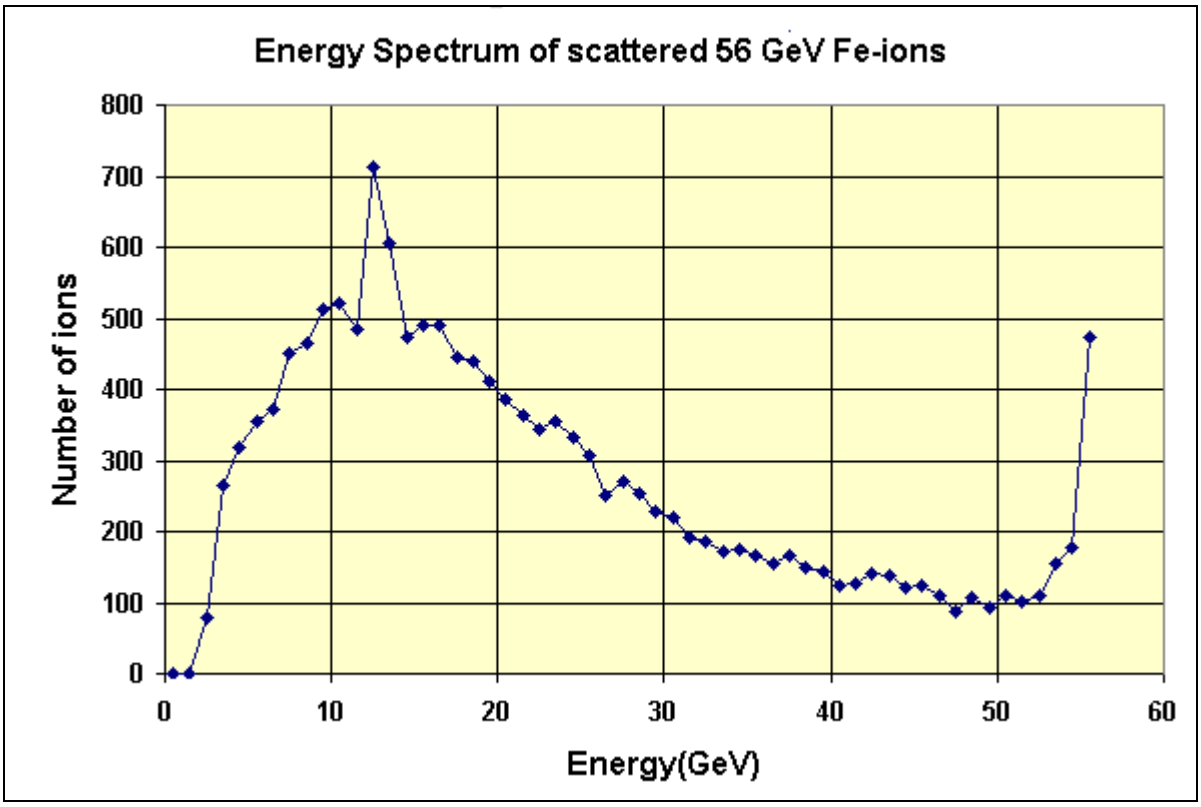

Fig. 17e Energy distribution of scattered ions for the case in which object jaws with 5μ peak-to-valley surfaces were simulated.

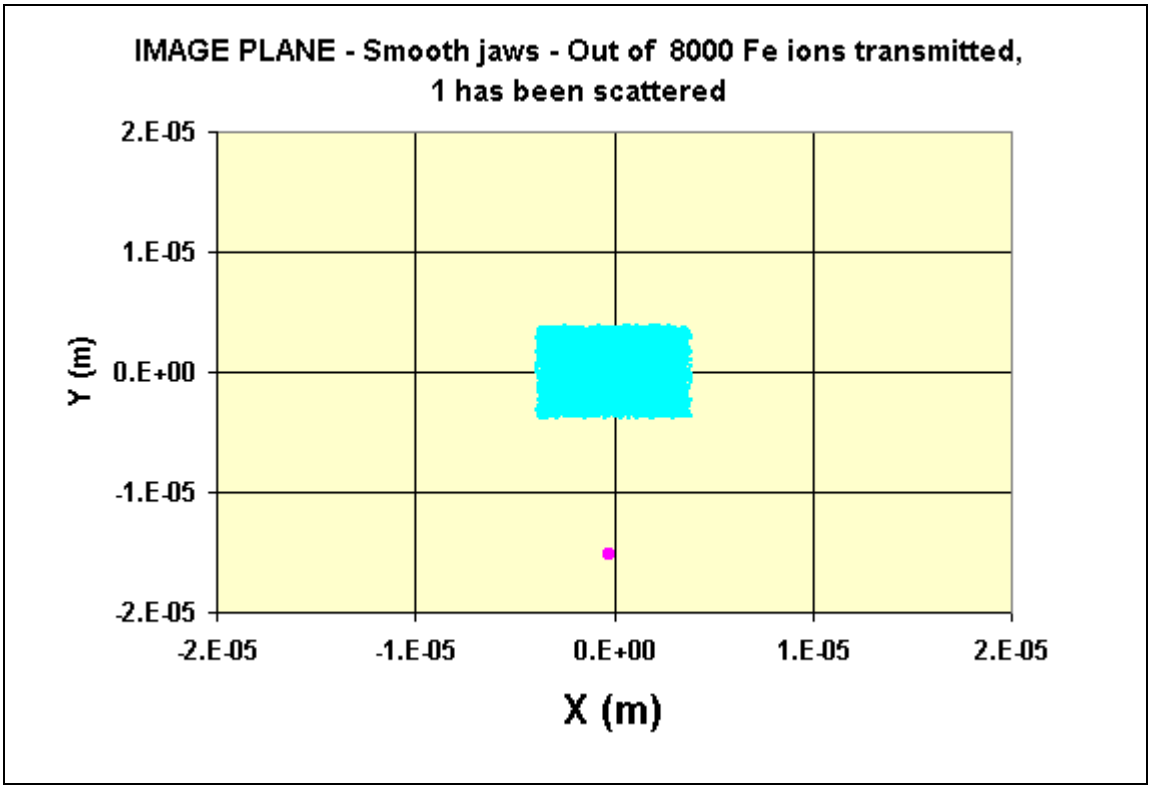

Fig. 18a The single ion appearing on the image plane that was scattered from smooth jaw surfaces is shown as a larger, purple dot. The energy lost by this ion was 170 MeV.

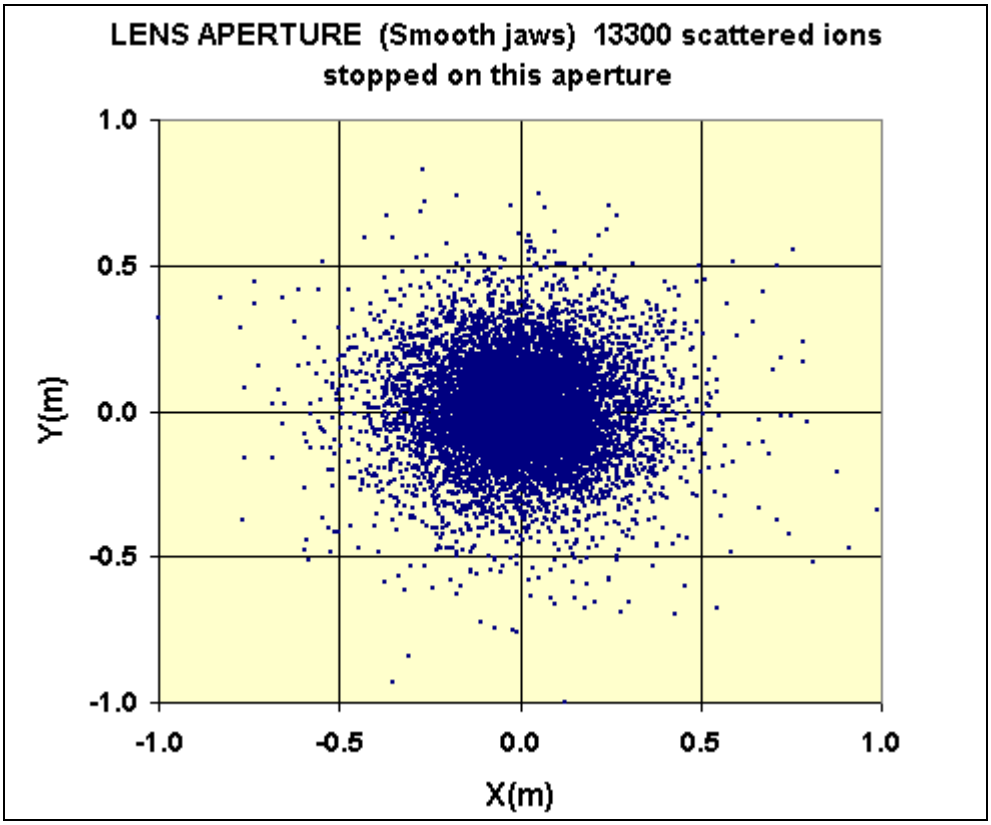

Fig. 18b Distribution of scattered ions stopped by the lens aperture for the case in which smooth object-jaw surfaces were simulated.

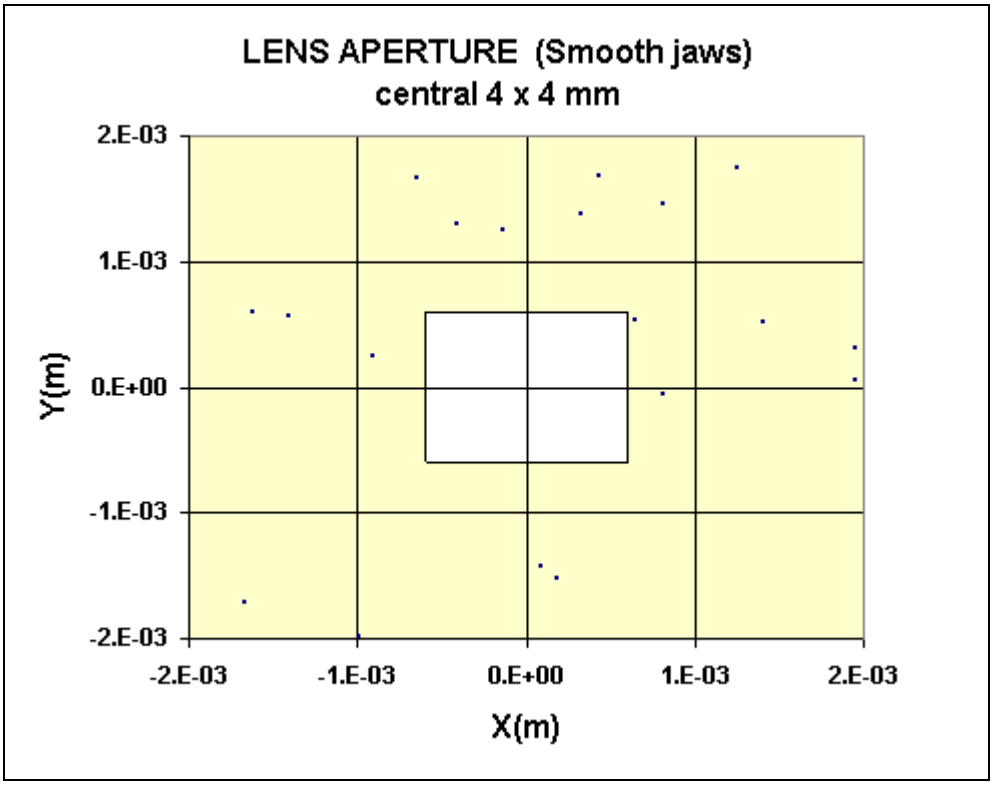

Fig. 18c The central 4×4 mm^2 of the distribution shown in fig. 18b. The 0.6×0.6 mm2 lens aperture is indicated by the square at the center.

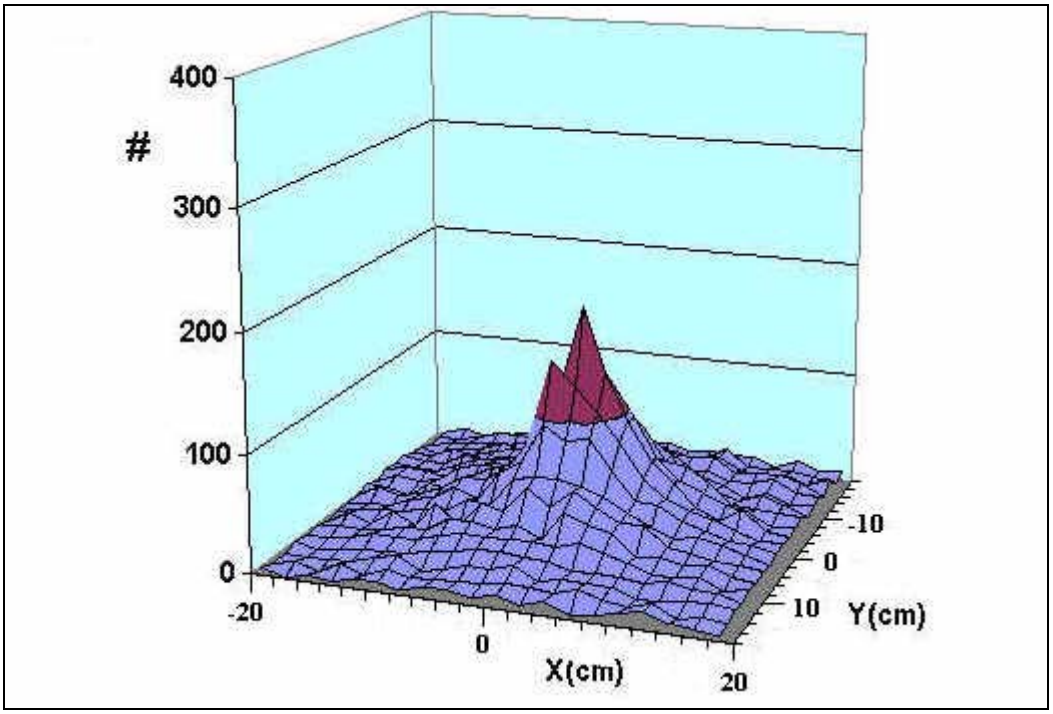

Fig. 18d 3-D view of the distribution of the 13,300 scattered ions stopped by the lens aperture for the case in which smooth object-jaw surfaces were simulated.

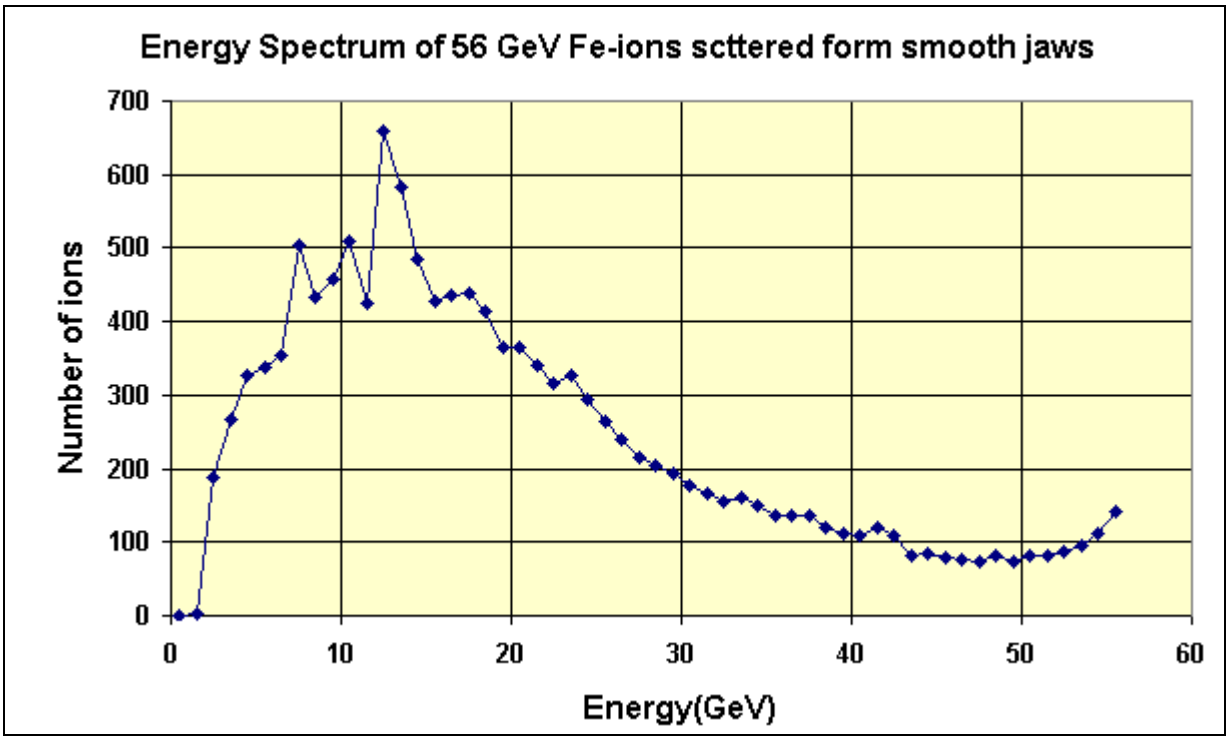

Fig 18e Energy distribution of scattered ions for the case in which smooth object-jaw surfaces were simulated.

From these results we see that the geometry chosen for this example is extremely effective in suppressing scattered ions from the image plane. Even for the worst case of 5μ peak-to valley object jaw surfaces (fig.17a), we get less than 0.5% scattered ions, most of them very close to the borders of the unscattered image and all of them within 0.04% of the full energy. A further large reduction of the number of scattered ions is available by using well-polished collimators (see fig. 18a). For the present example this improvement would be unimportant, but there will be other situations were it can become very significant.

The difference in scattering from smooth and not-smooth surfaces can also be clearly seen in the number and distribution of ions stopped by the lens aperture (see Figs. 17d and 18d). Not only are there more ions scattered for the not-smooth case but they are also more forward-peaked. But even in this case, the ion distribution on the lens aperture is wide enough so that very few ions come close to the opening (see Fig. 17c). This justifies not having considered multiple scattering in the lens aperture for the present example.

Much has been learned from this first simulation but there are several issues that need to be further addressed:

1) While it was shown that, for this example, scattering at the lens aperture isn't an issue, scattering at the field aperture hasn't yet been analyzed. The position of this aperture, the wide distribution of scattered ions and the extremely small acceptance of the object aperture would suggest that this isn't a problem, but one can't be sure. Intuition doesn't work very well when a few hundred scattered ions getting through, out of 10^9 incident ions, would be significant.

2) A significant fraction of the incoming ions will get fragmented in collisions with the material in the collimators. These are nuclear collisions that should result in angular distributions of the fragments which are wider than the distribution from atomic collisions considered by TRIM. Therefore the suppression of the fragments should be even more effective. The only caveat is that some of the lighter energetic fragments (such as protons and neutrons) will have much longer ranges than the heavier beam ions. This may lead to the need to increase the thickness of the collimators ore, more likely, to the introduction of additional radiation barriers with somewhat larger apertures. Beam cleanup through magnetic deflection is also possible but will hopefully not be necessary.

3) The effects of small misalignments of the object aperture and of the lens elements can and should be investigated to establish the appropriate tolerances which are anticipated to be challenging.

4) TRIM may soon undergo a revision[4)] to take into account finite nuclear size effects described by Lindhard and Sorensen [5)] which are expected to be significant at the relativistic energies of interest here. Multiple scattering predictions are not supposed to be affected [6)], but values of dE/dx may change. If such changes are significant the present calculations can be repeated using the forthcoming version of TRIM. Measurements at the Booster's NSRL line, however, indicate[7)] that values of dE/dx very close to the ones predicted by the present version of TRIM are obtained.

5) Magnetic shielding of the long drift space between the object aperture and the lens will probably be required to mitigate effects of stray AC and DC fields.

The preliminary results for the case analyzed here are very promising. It seems that we will indeed be able to take advantage of the low intensity (single hit) requirement to design a system with extremely small acceptance that effectively suppresses scattered ions while at the same time making efficient use of lenses of modest strength.

I would like to acknowledge useful comments and suggestions received from Kevin Brown, Veljko Radeka, Nick Tsoupas, Phil Pile, James Ziegler, Allan Sorensen and Marian Cholewa.

REFERENCES

1) "The Stopping and Range of Ions in Solids", by J. F. Ziegler, J. P. Biersack and U. Littmark, Pergamon Press, New York, 1985 (new edition in 2003).
2) J. F. Ziegler, http://www.srim.org/
3) Kevin Brown, private communication
4) J. Ziegler, private communication.
5) Lindhard and Sorensen, Phys.Rev.53A, 2443-2456 (1996)
6) Allan Sorensen, private communication
7) Phil Pile, private communication.